HCV Core protein needs triacylglycerols to fold onto the endoplasmic reticulum membrane

Dalila Ajjaji, Kalthoum Ben M'barek, Bertrand Boson, Mohyeddine Omrane, Ama Gassama-diagne, Magali Blaud, François Penin, Elise Diaz, Bertrand Ducos, François-Loïc Cosset, et al.

HCV Core protein needs triacylglycerols to fold onto the endoplasmic reticulum membrane

Dalila Ajjaji[1], Kalthoum Ben M'barek[1], Bertrand Boson[2], Mohyeddine Omrane[1], Ama Gassama-Diagne[3,4], Magali Blaud[5], François Penin[6], Elise Diaz[7], Bertrand Ducos[1,7], François-Loïc Cosset[2], Abdou Rachid Thiam[1]

[1] Laboratoire de Physique de l'École Normale Supérieure, ENS, Université PSL, CNRS, Sorbonne Université, Université de Paris, F-75005 Paris, France

[2] CIRI–Centre International de Recherche en Infectiologie, Univ Lyon, Université Claude Bernard Lyon 1, Inserm, U1111, CNRS, UMR5308, ENS Lyon, 46 allée d'Italie, Lyon, France

[3] INSERM, Unité 1193, Villejuif F-94800, France

[4] Université Paris-Sud, UMR-S 1193, Villejuif F-94800, France

[5] Université de Paris, CiTCoM, CNRS, F-75006 Paris, France

[6] Institut de Biologie et Chimie des Protéines, Bases Moléculaires et Structurales des Systèmes Infectieux, UMR 5086, CNRS, Labex Ecofect, University of Lyon, Lyon, France

[7] High Throughput qPCR core facility of the ENS, IBENS, PSL research University, F-75005 Paris, France

***Correspondence to**:
Abdou Rachid Thiam
Laboratoire de Physique,
Ecole Normale Supérieure,
PSL Research University,
75005 Paris Cedex 05, France
thiam@ens.fr

Abstract.

Lipid droplets (LDs) are involved in viral infections, but exactly how remains unclear. Here, we study the hepatitis C virus (HCV) whose Core capsid protein binds to LDs but is also involved in the assembly of virions at the endoplasmic reticulum (ER) bilayer. We found that the amphipathic helix-containing domain of Core, D2, senses triglycerides (TGs) rather than LDs *per se.* In the absence of LDs, D2 can bind to the ER membrane but only if TG molecules are present in the bilayer. Accordingly, the pharmacological inhibition of the diacylglycerol O-acyltransferase enzymes, mediating TG synthesis in the ER, inhibits D2 association with the bilayer. We found that TG molecules enable D2 to fold into alpha helices. Sequence analysis reveals that D2 resembles the apoE lipid-binding region. Our data support that TG in LDs promotes the folding of Core, which subsequently relocalizes to contiguous ER regions. During this motion, Core may carry TG molecules to these regions where HCV lipoviroparticles likely assemble. Consistent with this model, the inhibition of Arf1/COPI, which decreases LD surface accessibility to proteins and ER-LD material exchange, severely impedes the assembly of virions. Altogether, our data uncover a critical function of TG in the folding of Core and HCV replication and reveals, more broadly, how TG accumulation in the ER may provoke the binding of soluble amphipathic helix-containing proteins to the ER bilayer.

Introduction

Lipid droplets (LDs) regulate intracellular lipid storage and secretion via lipoproteins [1]. Pathogens or viruses often hijack these functions to replicate [1–4]. Indeed, viral infections often correlate with accentuated LD biogenesis or catabolism [1]: this is the case with many flaviviruses such as Dengue or Zika [5–9], hepacivirus such as hepatitis C (HCV) [10–13], enteroviruses such as polioviruses, herpes simplex virus type 1 (HSV-1) [8,14], or the severe acute respiratory syndrome coronavirus 2 [15,16]. How viruses interfere with the LD lifecycle is poorly understood.

LDs resemble lipoproteins or chylomicrons: they have a neutral lipid core composed of triacylglycerols (TG) and sterol esters, surrounded by a phospholipid monolayer containing proteins [17]. Many proteins associated with LDs have binding motifs found in apolipoproteins [18], such as amphipathic helices (AHs). Like lipoproteins, LD biogenesis occurs in the endoplasmic reticulum (ER) bilayer, yet, *via* a different mechanism [19]. Most LDs emerge into the cytosol [17,20] while lipoproteins assemble in the ER lumen [19].

The LD lifecycle starts with the synthesis of neutral lipids. For example, diacylglycerol O-acyltransferase 1 and 2 (DGAT1,2) generates TG, which is released in the hydrophobic core of the ER bilayer [21]. TGs are then freely mobile [22] but can condense to nucleate an LD that buds off into the cytosol and likely detaches from the bilayer [23]. At this stage, individual TGs may remain in the bilayer but at a concentration below the critical condensation concentration [24]. The cytosolic LD is tethered to the ER membrane by several factors such as Rab18 [25,26]. Following the action of the Arf1/COPI machinery, a subset of mature LDs reconnects to the ER, and the organelles may subsequently exchange lipids and proteins [23,27–29]. Finally, LD catabolism happens by the hydrolysis of TG by lipases such as adipose triglyceride lipase ATGL or lipophagy [30]. Fatty acids released during these processes are used for energy or making membranes or are re-esterified by DGAT1 to prevent lipotoxicity [31–33]. HCV viral proteins interfere with each of these steps of the LD lifecycle to promote efficient virus replication and secretion [11,12,34].

HCV remains a significant cause of chronic hepatitis, liver cirrhosis, and hepatocellular carcinoma [10]. It has a positive single-stranded RNA of 9.6 kb encoding a polyprotein precursor of ~3,000 amino acids. In infected liver cells, the polyprotein is processed by several viral and cellular proteases into ten proteins [35,36]: structural proteins (Core, E1, E2), which represent the major constituents of the viral particle, and non-structural proteins (p7, NS2, NS3, NS4A, NS4B, NS5A, NS5B). Among these, the Core protein of the capsid and NS5A localize to the LDs' surface using AH motifs [37,38]. For the JFH1 HCV, the binding of Core to

LDs is critical for the production of HCV virions [39,40], often referred to as ‘lipoviroparticles’ harboring neutral lipids as well as apolipoprotein B or E [37,41]. The exact functions of LDs in the assembly and secretion of HCV virions are still elusive.

Core is a 191 amino acid-long peptide harboring (Figure 1A) an N-terminal hydrophilic D1 domain, a D2 domain of 42 amino acids containing two AHs bridged by a small disordered loop (Figure 1B), and a transmembrane D3 domain of 20 amino acids at the C-terminal, serving as a signal peptide [35,42]. This immature form of Core is anchored to the ER bilayer by D3. Cleavage of D3 by the cellular Signal Peptide Peptidase (SPP) yields mature Core, made by D1D2 (Figure 1A), which localizes to LDs by D2 [10]. Intriguingly, D1D2 needs to associate with the ER membrane to participate in the virions’ assembly [43–45]. It is unknown if D1D2 binds directly to the ER and/or traffics between LDs to the ER bilayer to assemble virions. We sought to address this question in this paper.

Results

Mature Core and D2 preferentially bind to LDs over the ER bilayer.

Core is translated at the N-terminus of the viral polyprotein and released after two successive cleavages by cellular proteases. The first cleavage generates an immature Core, D1D2D3 (Figure 1A). The second cleavage, just before D3, releases mature Core D1D2 (hereafter Core) from the ER bilayer. D1D2 binds to LDs by the AHs of D2 (Figure 1B) [38,39,42].

To investigate the localization of Core to LDs vs. ER, we used the hepatocarcinoma Huh7 model cell line and co-expressed mCherry-sec61ß, an ER marker, with JFH1-D1D2D3. Next, the cells were fed with oleic acid (OA) for 24hr to induce LDs, then fixed and immunostained (IF) for Core. Core was on all LDs as previously shown [3,39,46] but did not display a noticeable ER localization (Figure 1C). This observation indicates that cleavage at D3 occurred, and Core, i.e., D1D2, was released but incapable of binding to the ER bilayer, at least not as efficiently as to LDs.

To confirm Core localization, we expressed D1D2 directly instead of D1D2D3 but could not detect any protein signal by IF. D1D2 is highly prone to proteasomal degradation [47]. When we treated the cells with the protease inhibitor MG132, before D1D2 overexpression, we found by IF that D1D2 was in the nucleus (Figure 1D, Figure S1A). Such nuclear localization is mediated by interaction with the importin-PA28 complex and signatures Core's degradation [47]. Indeed, several nuclear localization signals were previously identified in D1 [48].

Together, the above results support the model that when cleavage happens at D3, a fraction of Core, which is soluble, is stabilized by LDs and escapes degradation into the nucleus. The discrepant localization of Core upon the expression of D1D2D3 and D1D2 likely pertains to kinetics reasons. In D1D2, the protein is directly released in the cytosol and imported to the nucleus. In D1D2D3, a fraction of Core could also be released and imported to the nucleus. However, the initial docking of the protein to the ER bilayer, close to LDs, may facilitate its rapid binding and stabilization to LDs.

To get more insights into Core's localization, we focused on D2, missing the nuclear import signals present in D1. eGFP-D2 displayed a localization similar to Core: it was cytosolic, localized to all LDs but not to the ER bilayer (Figure 1E, Figure S1B). This observation was confirmed in HeLa cells, which have fewer or no LDs in non-fed conditions: eGFP-D2 was soluble and sometimes presented aggregates; in OA feeding, it was on LDs and did not show a noticeable ER signal (Figure S1C).

Finally, to better visualize the ER membrane and know whether D2 binds to it, we added a hypotonic culture medium to the cells (Figure 1F) to induce the formation of Giant intracellular ER vesicles (GERVs) [22,49,50], offering a higher spatial resolution (Figure 1F). We transfected the Huh7 cells with eGFP-D2 and ER-BFP, marking the ER lumen, and induced intracellular GERVs (Figure 1G, Figure S1D). We found a clear D2 signal around LDs but not on the surface of the intracellular GERVs, agreeing with our above findings that D2, and likely Core, cannot directly bind to the ER membrane. Contrasting with this behavior, when we repeated the experiment with eGFP-Plin1, we found a signal on both intracellular GERVs and LDs [51] (Figure 1H, Figure S1E), albeit a higher signal was on the latter.

D2 preferentially folds onto droplets deficient in phospholipids

We used a reductionist approach to validate our findings. Within a single glass chamber, we added both TG-in-buffer droplets and giant unilamellar vesicles (GUVs) made of dioleoyl phosphatidylcholine (DOPC) and dioleoyl phosphatidylethanolamine (DOPE), at a ratio of 70/30. We then injected purified JFH1-eGFP-D2 and found its exclusive recruitment to the droplets, not the GUV bilayers (Figure 2A,2C). This behavior contrasted with the rhodamine-tagged AH of NS5A-HCV that was efficiently bound to both droplets and bilayers (Figure 2B,2C). The less-selective binding of the NS5A-AH likely pertains to its multiple bulky hydrophobic residues [52], compared with D2 (Figure S2A).

To confirm that the folding of D2 AHs mediated the binding to the TG/buffer interface, we used circular dichroism to determine the presence of alpha-helices. We prepared TG-in-buffer droplets by bath sonication in the presence of 0.1 DOPC in TG (w/w to TG); in parallel, we prepared DOPC liposomes by ultra-power sonication, yielding nanometric vesicles. We then used a synthesized J6-D2 peptide and performed circular dichroism experiments with both solutions. No alpha helix signal was noticed when the peptide was alone in the buffer (Figure 2D,2E). Alpha-helices' signal appeared in the presence of droplets (Figure 2D) unless these were highly covered with phospholipids (Figure S2B).

In contrast, alpha-helices were barely detectable with liposomes, independently of liposome size (Figure 2E, S2C). This data supports that D2 folds better when TG is exposed, which agrees with the above *in vitro* and cellular studies. Photobleaching experiment of D2 on the TG-in-buffer droplets showed a slow recovery, indicating that D2 firmly folds onto this interface (Figure 2F, Figure S2D).

Since by circular dichroism we found that the phospholipid level influenced D2 folding (Figure 2D, S2B), we probed by fluorescence how the monolayer phospholipid density impacts D2 binding to the model LDs. We made artificial TG-in-buffer droplets covered by different DOPC

levels, reported by the rhodamine-DOPE (Rhod-PE) used at 1% (w/w to DOPC) and serving as a phospholipid marker (Figure 2G, S2E). The droplets were then introduced in a chamber, and purified JFH1-eGFP-D2 was added. We observed a non-uniform signal distribution between droplets (Figure 2H). D2 associated better with droplets containing less DOPC, providing more access to TG (Figure S2E, S2F, Figure 2I). This restriction of binding by DOPC was more drastic on D2 than the AH of Caveolin1 [53]. Therefore, the LD phospholipid coverage can finely tune D2 binding; a tight cover will prevent D2 binding despite its strong association with bare TG/water interface (Figure 2I), agreeing with the circular dichroism results (Figure S2B).

Taken together, our results indicate that Core can bind alone to LDs and not to the ER bilayer. The AHs of D2 fold and remain firmly attached to TG/aqueous interfaces, and this binding capacity is dependent on the phospholipid monolayer density.

D2 competes off Perilipin 3 and not 2 for associating with LDs

Like phospholipids, proteins on LDs can also have a barrier function and prevent the non-specific recruitment of proteins [54,55]. In the Huh7.5 liver cells, perilipin (Plin) 2 and 3 are the most abundant LD protein coats and Plin1 is not expressed [56]. When these cells were transfected with mCherry-Plin1-3, the proteins perfectly localized to the LD surface (Figure S3A). To test whether they interfere with D2 binding, we did a competition assay wherein JFH1-eGFP-D2 is co-expressed with the mCherry-Plins [51,55]. After 24h of co-transfection and OA supply, the cells were visualized under the same imaging settings (Figure 3A). We took cells presenting similar D2 and Plin levels based on their bulk signals. Then, we determined the protein fluorescence intensity on the LDs and subtracted the surrounding background signal. The highest protein signal was then set to 1, to compare better the relative recruitment of D2 vs. Plins.

We found that D2 almost systematically excluded Plin3 from the LDs' surface under our working conditions (Figure 3A-C) (24hr after OA loading); this exclusion was neat on nuclear LDs (Figure 3A, arrowheads), presenting fewer LDs and a lower Plin3 background. D2 colocalized with Plin2 on LDs, and there was no noticeable exclusion between the two proteins (Figure 3A-C), even on nuclear LDs (Figure 3A, arrowhead). Finally, Plin1, which is absent in the liver and has a higher binding affinity to LDs than Plin2,3 [51], greatly displaced D2 from LDs (Figure 3A-C). This binding exclusion of Plin1 was validated *in vitro* by the eviction of D2 by Plin1 from shrinking TG-buffer interfaces (Figure S3B, S3C) [55]. This observation was also true for JFH1-Core, which was displaced from LDs by Plin1 (Figure S3D).

D2 firmly bound the bare TG/buffer interface *in vitro* (Figure 2F, Figure S2D). To get insights into its binding stability to LDs, we performed photobleaching experiments. We found different recovery kinetics between LDs from different cells highly expressing D2 (Figure 3D, S3E): the majority of LDs had a rapid characteristic recovery time (<20sec), and few LDs recovered more slowly (> 20sec) (Figure 3E). eGFP is soluble, bigger than D2, and could provoke the rapid fall-off of D2. To rule this out, we designed constructs where eGFP is bridged to D2 by flexible glycine linkers, eGFP-GGGGS-D2 and eGFP-$(GGGGS)_2$-D2. These proteins displayed similar behavior to eGFP-D2, i.e., cytosolic and recovered rapidly on most LDs (Figure S3F, S3G). This observation supports that eGFP was not responsible for the rapid dissociation of D2 from LDs. Lastly, even within a single cell, D2 showed different recovery rates between LDs (Figure 3F, Movie), indicating that an LD subset provides a more stable binding to D2.

In conclusion, the above data support that Core can alter the proteome of LDs and, possibly, LD functions. Strongly LD-associating proteins can compete and prevent D2 from accessing TG. Finally, a subpopulation of LDs more than others appears to better stabilize D2.

Arf1/COPI inhibition decreases Core recruitment to LDs and lipoviroparticles.

Our above findings show that the surface coverage level of LDs modulates the binding of Core/D2, which more stably occurred on an LD subset. Interestingly, the Arf1/COPI machinery, involved in the budding of vesicles from the Golgi apparatus for retrograde cargo trafficking, acts also on an LD subpopulation; it modulates the surface accessibility of these LDs to proteins [23,27]. For instance, the inhibition of Arf1/COPI impedes the binding to LDs of ATGL [57,58], GPAT4 [23], Plin2 or ADRP, but not Plin3 or TIP47 [57]. Thus, we probed whether Arf1/COPI inhibition prevents Core binding to LDs.

To block Arf1/COPI action, we used Brefeldin A (BFA), which inhibits the activity of the guanine exchange factor of Arf1, GBF1, and the assembly of the machinery. We loaded Huh7 cells with OA for 24hr to increase LDs, treated them with BFA, and transfected them with Core-D1D2D3 before imaging, after 24hr. Compared to control cells, BFA decreased Core association with LDs and promoted localization to the nucleus (Figure 4A-B, S4A), reminiscent of D1D2 localization when directly expressed (Figure 1D). This nuclear localization probably arose from the redirection of Core from LDs or the ER to the nucleus where it is degraded [47]. We also observed another phenotype where some LDs had a complete Core signal, few others completely lacked it, while others displayed arc signals (Figure 4A, Figure S4A-B), as similarly seen previously [45]. Small and medium LDs, <2µm in size, were more impacted than larger ones (Figure 4C). The arc feature may reveal the onset of LD-ER or LD-Golgi contacts excluding Core [59]; alternatively, it could be the signature of LDs that did not fully emerge into

the cytosol [20], as seen with the appearance of apoB crescent shapes when apoB is overexpressed in Huh7 hepatocyte cells [60]. In summary, the activity of GBF1 is necessary for the correct binding of Core to LDs and its non-degradation.

We repeated the above experiment with D2 and obtained the same phenotype (Figure 4D). Within a single cell, D2 was on an LD subset, or displayed arc features, or was utterly absent from LDs. The arc and ring signals of D2 recovered very rapidly following photobleaching, showing that such signals did not correspond to a firm binding to the LDs (Figure S4C). We also observed other phenotypes wherein D2 is absent from LDs and, instead, formed puncta in the cytosol. This phenotype is also reminiscent of mature Core's nuclear localization in BFA treatment (Figure 4A, S4A). Indeed, since D2 lacks D1, it could not be targeted to the nucleus for degradation but was prone to aggregation. As D2 is a basic soluble peptide, unlikely to possess any biological function, the above observations support that BFA treatment decreased the LD surface accessibility to proteins.

Since BFA principally interferes with GBF1, which activates Arf1, we decided to target the COPI coatomers. We used siRNAs against the ßCOP subunit. We transfected JFH1-Core in Huh7 cells pre-treated with the siRNAs for 24hr (Figure 4E, Figure S4D-E). The impact of the siRNA treatment was noticeable through the loss of the compactness of the Golgi, which was more fragmented (Figure S4F). Similar to previously shown, the reduction of βCOPI decreased the levels of Core [61] (and also ADRP [57]) (Figure S4E) but, consistent with our hypothesis, it led to impaired binding of Core to LDs and yielded phenotypes similar to BFA (Figure 4E-F,S4D-F) [45].

Since we found that Arf1/COPI inhibition decreased Core association with LDs, we wondered how this would impact the production of lipoviral particles. We infected Huh7 cells with Jc1 HCV chimera and analyzed Core localization by IF, with or without OA addition (Figure S4G). Core was barely found around LDs in the absence of OA (Figure S4H). Instead, LDs were more extensive when OA was added and they had a clear Core signal at their surface (Figure S4H). This observation suggests that when more TGs are made, Core has higher chances to interact with LDs. Under the same infection and OA feeding conditions, if Plin1, in contrast to Plin2 or 3, was overexpressed to mask the LD surface, Jc1-Core binding to LDs was drastically diminished (Figure S4I); this result agrees with our previous competition experiments (Figure 3B).

Next, we analyzed the intracellular and extracellular lipoviral particles made at 24h post-infection. Shortly after infection, without OA, the infectious virions were mainly found

intracellularly (300 FFU/mL versus less than 100 FFU/mL for the extracellular infectious virions) (Figure S4J). On the opposite, in OA-treated cells, the amount of intracellular infectious particles was negligible (less than 20FFU/mL) compared with the extracellular one (500 FFU/mL) (Figure S4J). This data indicates that secretion of HCV particles was highly stimulated when TG biosynthesis is stimulated by OA addition. It highlights the importance of TG for an efficient virion secretion.

Finally, we determined the impact of Arf1/COPI in the OA feeding condition. At eight hours post-infection, cells were treated with BFA for 16hrs and then fixed (Figure 4G). Core was found predominantly on LDs' surface in control cells but much less in BFA-treated ones (Figure 4H). In the latter, we found a drastic reduction in the number of assembled virions, both intracellularly and extracellularly, below the detection threshold, respectively, of 50 and 10 FFU/mL (Figure 4I). Finally, washing out BFA led to the relocalization of Core to LDs and the efficient re-assembly of lipoviral particles (Figure S4K-L), confirming the crucial role of Arf1/COPI in the assembly of HCV virions.

Triacylglycerols recruit D2 to the ER membrane

Core is required for the assembly of lipoviral particles that takes place at the ER membrane. A question is how the binding of Core to LDs relates to this assembly process at the ER bilayer. Our above results showed that D2 associates firmly with TG/water interfaces, on LDs. However, the ER membrane, the biosynthesis site of neutral lipids, can also bear TG molecules, especially when LD assembly is impaired or delayed [22,62,63]. Thus, we hypothesized that the presence of TG could promote D2 binding to the ER bilayer. Such binding would guarantee Core's presence at the ER for the assembly of virions. To test our hypothesis, we worked with intracellular giant ER vesicles (GERVs) to gain spatial resolution of the ER membrane, and TG and D2 localization [50]. We chose Cos7 cells because they barely present LDs, unless they are cultured in an energy-rich media, and we can monitor TG biosynthesis [22] and D2 localization (Figure 1F-H).

We transfected the cells with eGFP-D2 and induced intracellular GERVs, marked by RFP-KDEL (Figure 5A, S5A-B) or BFP-ER (Figure 5B). Consistent with our data in Figure 1G, D2 was absent from the intracellular GERVs' surface and was cytosolic (Figure 5A-B, Figure S5A-B). Then, we fed the cells with OA, supplemented with OA-C12-BODIPY, to induce the biosynthesis of fluorescent TG molecules and their accumulation into the GERVs' membranes [22]. To also report for the GERVs' membrane hydrophobicity by the presence of neutral lipids, we used LipidTox in the system [22] (Figure 5A, S5C). We observed an OA signal in GERVs, likely fluorescent TG, which was strikingly concomitant with a clear binding of D2 (Figure 5A-

B, S5A-B). The level of D2 on the neutral lipid-rich intracellular GERVs increased with the LipidTox signal (Figure 5C, S5C). These results strongly agree with our model that the binding of D2 to GERVs is promoted by the biosynthesis and accumulation of TG in the bilayer (Figure 5D).

To ensure that the localization of D2 to the GERVs' membrane was due to TG accumulation within the bilayer (Figure 5D), we repeated the experiment but with pre-treating the cells with DGAT1,2 inhibitors to block TG synthesis (Figure S5D-G). Under this condition, when the intracellular GERVs were fed with OA, as previously, the LipidTox GERV signal was barely visible and the binding of D2 to the GERVs was severely impaired (Figure 5E-F, Figure S5E-G). This data also support that the presence of TG in the ER bilayer mediated the recruitment of D2 to the GERV bilayers.

Next, we did photobleaching experiments of D2 on GERVs containing TG. On randomly picked GERVs from different cells, the D2 recovery rate was lower than on cellular LDs (Figure 5G-H, S5I), but it was still faster than on bare TG/buffer interfaces (Figure 2F). We interpret this data as if the protein coverage of the GERVs was sparser than on LDs, possibly due of the swelling process. As a consequence, TG was more exposed and accessible to D2 on these GERVs. Consistent with this interpretation, when we overexpressed mCherry-sec61ß, an integral ER membrane protein, instead of mCherry-KDEL or ER-BFP, which mark the ER lumen, the binding of D2 to GERVs was significantly reduced despite the OA addition (Figure 5I). The lower the mCherry-Sec61ß on GERVs, the higher the eGFP-D2 signal (Figure 5J, Figure S5J); GERVs with higher LipidTox signals still recruited more D2 (Figure S5J). Based on this observation, we concluded that mCherry-Sec61ß competed off D2 from GERVs, exactly as Plin1 did on LDs (Figure 3B).

Altogether, these data indicate that TG molecules, independently of their organelle localization, can recruit Core. They seem to stabilize the binding of Core to the ER membrane, which is a necessary condition for the assembly of lipoviral particles.

D2 binds to bilayer membranes physically connected to TG droplets

Although TG molecules in GERVs favored D2 recruitment, it could be via indirect mechanisms. To directly test our model that TG molecules infused in the ER bilayer can recruit D2, we turned to *in vitro* reconstitution with droplet-embedded vesicles (DEVs) [64]. DEVs consist of a neutral lipid droplet embedded in a giant unilamellar vesicle (GUV) [65], here made of DOPC:DOPE (70: 30) and triolein (Figure 6A). We used rhodamine-PE to visualize the bilayer and monolayer interfaces. Next, we added eGFP-D2 to the DEV solution and followed its localization. D2 was

recruited to the TG droplet and not the bilayer (Figure 6A, S6A), in contrast to NS5A-AH that bound to both (Figure S6B). A droplet monolayer has a lower phospholipid packing than a bilayer, even though they are in contiguity [53,66]. This discrepancy might explain the exclusive recruitment of D2 to the monolayer (Figure 6A).

When the surface tension of DEVs is increased, TG molecules partition from the droplet to the bilayer [67,68]. We used this strategy to increase TG levels in the bilayer and determine if this would favor D2 recruitment to the bilayer, as seen with GERVs. After D2 bound to the droplet of DEVs, we increased the bilayer tension by adding water to the bulk medium (Figure 6B) to provoke the system's swelling and the delivery of TG to the bilayer [68]. In the course of swelling, reported by the increase in the DEV radius, D2 increasingly bound to the DEV bilayer region (Figure 6B). Thus, TG molecules released by the droplet to the bilayer likely recruited D2. As a control, we induced the swelling of a bare GUV and we did not observe the recruitment of D2 to the bilayer (Figure 6C), even if the latter is stretched to its maximum level. In the DEV swelling experiment, the bilayer-localized D2 might come from the direct binding of D2 from the bulk solution to the bilayer or the lateral diffusion of D2 from the droplet surface to the bilayer. In the latter case, D2 could carry TG from the droplet surface to the bilayer.

Collectively, our *in vitro* results with DEVs and cell data with GERVs indicate that TG molecules in the bilayer recruit and stabilize Core/D2 to the ER membrane.

D2 has sequence similarities with apoE and a preference for TG

Based on our above observations, we hypothesized that D2 has an affinity for TG. Since Core assembles into lipoviral particles containing ApoE or ApoB [37,69], we asked whether D2 shares features with apolipoproteins. Sequence alignments of Core with apolipoproteins revealed conserved regions between JFH1-Core and ApoE. Namely, we found conserved regions between Core-D1 and ApoE (Figure S6C, S6D) and more substantial similarity between Core-D2 and the lipid-binding domain of ApoE [18], i.e., the hydrophobic loop and portion of their AHs involved in their association with TG/buffer interfaces (Figure 6D). Phylogenetic tree analysis shows that D2, in contrast to the 11-mer repeats of perilipins, clusters with apoE, apoC1, and the non-structural protein 1 of Dengue virus (Figure S6E), all binding to TG/water interfaces. Based on this analysis, we decided to test whether D2 prefers TG as compared with apoE.

To study the affinity of D2 for TG, we used a tensiometer approach [51,70]. We generated oil-in-water droplets made either of TG or squalene, an intermediate neutral lipid in sterol biosynthesis, and added the same concentration of J6-D2. Recruitment of D2 would be

accompanied by a decrease in surface tension to an equilibrium value (Figure 6E) [51,70]. We found a reduction of tension that was much more striking for TG, from ~34 to ~11 mN/m, than for squalene, from ~22mN/m to ~20mN/m, indicating that D2 was barely recruited to the squalene/buffer interface (Figure 6F, 6G). We looked at the behavior of apoE, and it decreased TG's surface tension as efficiently as for squalene (Figure 6G, S6F). These observations support that D2 has a higher affinity for TG than for squalene and, also, a higher capacity to distinguish the neutral lipid/water interfaces than apoE. In contrast to D2, apoE does not only have the lipid-binding domain but also possesses multiple AHs forming a four-helix bundle that unzips and associates with membranes [18] (Figure S6C). These AHs might induce the strong binding of ApoE to the neutral lipid/water interface, regardless of the neutral lipid chemistry or composition.

Discussion

The binding of Core to LDs facilitates the assembly of HCV viral particles. However, this assembly occurs at the ER membrane bilayer and implicates also Core. Thus, Core protein has to relocalize from LDs to the ER bilayer or bind directly to the latter. It is unknown how such traffic happens.

We found that Core's LD-binding domain, D2, shares sequence similarities with the lipid-binding part of apoE and likely has an affinity for TG. We propose that mature Core stably binds to the surface of a subset of LDs from which it relocalizes to ER regions where virions assemble (Figure 7A). This relocation might be assisted by other HCV viral proteins such as p7-NS2 [46]. If LDs are absent or physically disconnected from the ER, Core may still localize itself to the ER but would require the presence of TG in the membrane (Figure 7B). Such an ER targeting mechanism appears so far uncommon for AH-containing proteins commonly binding to LDs. An exception might Plin3, which may associate with the ER bilayer when diacylglycerol levels in the membrane increases, for example, during the early steps of LD biogenesis [71]. All these observations highlight a possible role for ER membrane-infused neutral lipids in recruiting soluble proteins to the membrane.

Why does Core bind to LDs and not the ER, following the SPP-mediated cleavage at the D2-D3 region? A first answer is that the free TG concentration in the ER should be low under normal conditions, since most TGs are packaged into LDs. Thus, Core may not be able to directly bind the ER, as we found in Figure 1,5. Since LDs are less packed with phospholipids than the ER bilayer [53], their hydrophobic TG core is more accessible to soluble proteins and allows the efficient folding of D2 onto LDs (Figure 2, S2). In this picture, the LD surface acts as a protein folding partner for AHs and induces Core interfacial stabilization (Figure 7A). A second answer is that the stable binding of Core to LDs prevents its nuclear import and subsequent degradation (Figure 7A). In this view, LDs safeguard Core for degradation. In the meantime, LD-bound Core serves as encapsidation machinery of the viral HCV RNA [43,44,72–74]. Lastly, during the assembly of HCV particles, Core may stably move from LDs to the ER bilayer, through ER-LD bridges [29,75], and carry TGs from the LD to the nascent virion assembly site (Figure 7A). In this scheme, LDs would serve as a TG seed used by Core for the assembly of virions.

In the absence of LDs, or when LDs are disconnected from the ER, viral particles may still be assembled but only if TG molecules are present within the ER bilayer (Figure 7B). Indeed, if Core binds to TGs at the ER membrane, all HCV components that are required to assemble lipovirions (i.e., E1, E2, Core, TG) would be available in the same place. Therefore, proteins

involved in regulating TG fluxes between ER and LDs [76], such as proteins involved in LD assembly or ER-LD connection should alter HCV particles' assembly. In the absence of TG from the ER, the inability of Core to bind to the membrane and its subsequent degradation should decrease infection (Figure 7C-D). Interestingly, DGTA1 inhibition, leading to decreased lipogenesis, noticeably reduced virions [77]. Accordingly, we found that the inhibition of DGATs' activity prevented Core localization to the ER bilayer (Figure 5D)

Core displaces Plin3 from the LD surface, indicating that it may perturb the LD proteome and liver lipid metabolism, as corroborated by several observations. Core binding spatially redistributes LDs by highjacking microtubules and dynein [78] and, thereupon, interferes with lipid metabolism [79,80]. Core binding to LDs is inhibitory for the lipolytic activity of ATGL [81] and, hence, increases cellular TG levels, a favorable condition for the binding of Core and virion assembly (Figure 4H-I, S4H,S4J). Also, Core interferes with other proteins involved in TG synthesis and packaging into LDs or degradation. An example is its interaction with DGAT1 [77]. It may modulate DGAT1 activity to ensure the presence of TG in the ER or directly bind to DGAT1-released TGs [21]. Likewise, Rab18, an essential cellular component of LD assembly, is also used by Core for targeting membranes [82]. Finally, HCV also highjacks the lipophagy pathway [9,83], which, through re-esterification of fatty acids into TG in the ER [31,32], may favor for Core recruitment to the ER membrane. These examples illustrate how HCV may interfere with TG metabolism and packaging to grease the ER membrane for the stable binding of Core and the efficient assembly of virions.

Arf1/COPI keeps the surface of LD accessible to proteins [23]; its inhibition prevents the relocalization of proteins from the ER, or the cytosol, to the surface of LDs [23,57,58]. Accordingly, Arf1/COPI inhibition reduced Core binding to LDs (Figure 4A-E). Consequently, we more often found Core in the nucleus where it is degraded (Figure 7). The occurrence of this degradation may explain the decreased Core levels upon Arf1/COPI inhibition (Figure S4E). Arf1/COPI also favors LD-ER physical contiguity [23,27]; its inhibition prevents the exchange of proteins between the two organelles [23]. Therefore, in addition to reducing Core association with LDs, Arf1/COPI inhibition may prevent the relocation of Core from the surface of LDs to the ER membrane. Hence, even though the RNA levels of Core is decreased by Arf1/COPI inhibition [61], the inability of the protein to efficiently access TG in LDs and the ER membrane likely accounts for the severe decrease in the number of assembled virions (Figure 4H-I). It is interesting to quote that Arf1/COPI inhibition also prevents the association of the Dengue virus capsid proteins with LDs [84]. Therefore, our findings may represent a general principle by which the LD surface and ER-LD contacts serve as a folding hub for some viral proteins, which may sense and use TG to promote viral assembly.

In conclusion, our results offer a crucial picture of molecular mechanisms governing the cellular localization of HCV Core protein. They provide a complementary avenue for developing drugs against HCV and related viruses by preventing viral proteins from modulating and accessing TG in LDs or the ER membrane.

ACKNOWLEDGMENTS

We are thankful to all the group members for their valuable comments and critical read of the manuscript. This work was supported by the Agence Nationale de Recherches sur le Sida et les Hépatites Virales (ECTZ7095) to ART.

Competing interests

The authors declare no competing interests.

Author contributions

The research was designed by ART, with FLC, BB, FP, AGD, and DA. DA performed all cellular and in vitro experiments with the assistance of KBM, MB, and MO. BD and ED generated the recombinant constructs and plasmids of the proteins. BB and FLC led the virology experiments. DA and ART wrote the manuscript, reviewed by all co-authors.

1. Vieyres G, Pietschmann T. HCV pit stop at the lipid droplet: Refuel lipids and put on a lipoprotein coat before exit. Cells 2019;8:233.

2. Daniel J, Maamar H, Deb C, Sirakova TD, Kolattukudy PE. Mycobacterium tuberculosis uses host triacylglycerol to accumulate lipid droplets and acquires a dormancy-like phenotype in lipid-loaded macrophages. PLoS Pathog 2011;7:e1002093.

3. Miyanari Y, Atsuzawa K, Usuda N, Watashi K, Hishiki T, Zayas M, Bartenschlager R, Wakita T, Hijikata M, Shimotohno K. The lipid droplet is an important organelle for hepatitis C virus production. Nat Cell Biol 2007;9:1089–1097.

4. Pereira-Dutra FS, Teixeira L, de Souza Costa MF, Bozza PT. Fat, fight, and beyond: The multiple roles of lipid droplets in infections and inflammation. J Leukoc Biol 2019;106:563–580.

5. Samsa MM, Mondotte JA, Iglesias NG, Assunção-Miranda I, Barbosa-Lima G, Da Poian AT, Bozza PT, Gamarnik AV. Dengue virus capsid protein usurps lipid droplets for viral particle formation. PLoS Pathog 2009;5:e1000632.

6. Martin-Acebes MA, Vazquez-Calvo A, Saiz J-C. Lipids and flaviviruses, present and future perspectives for the control of dengue, Zika, and West Nile viruses. Prog Lipid Res 2016;64:123–137.

7. Martín-Acebes MA, Jiménez de Oya N, Saiz J-C. Lipid metabolism as a source of druggable targets for antiviral discovery against Zika and other flaviviruses. Pharmaceuticals 2019;12:97.

8. Monson EA, Crosse KM, Duan M, Chen W, O'Shea RD, Wakim LM, Whelan DR, Helbig KJ. Intracellular Lipid Droplet Accumulation Occurs Early Following Viral Infection and Is Required for an Efficient Interferon Response. bioRxiv 2020;

9. Zhang J, Lan Y, Li MY, Lamers MM, Fusade-Boyer M, Klemm E, Thiele C, Ashour J, Sanyal S. Flaviviruses exploit the lipid droplet protein AUP1 to trigger lipophagy and drive virus production. Cell Host Microbe 2018;23:819–831.

10. Roingeard P, Hourioux C. Hepatitis C virus core protein, lipid droplets and steatosis: HCV core, lipid droplets and steatosis. J Viral Hepat 2007;15:157–164.

11. McLauchlan J. Lipid droplets and hepatitis C virus infection. Biochim Biophys Acta BBA - Mol Cell Biol Lipids 2009;1791:552–559.

12. Popescu C-I, Riva L, Vlaicu O, Farhat R, Rouillé Y, Dubuisson J. Hepatitis C virus life cycle and lipid metabolism. Biology 2014;3:892–921.

13. Lavie M, Dubuisson J. Interplay between hepatitis C virus and lipid metabolism during virus entry and assembly. Biochimie 2017;141:62–69.

14. Laufman O, Perrino J, Andino R. Viral generated inter-organelle contacts redirect lipid flux for genome replication. Cell 2019;178:275–289.

15. Dias S da SG, Soares VC, Ferreira AC, Sacramento CQ, Fintelman-Rodrigues N, Temerozo JR, Teixeira L, Nunes da Silva MA, Barreto E, Mattos M. Lipid droplets fuel SARS-CoV-2 replication and production of inflammatory mediators. PLoS Pathog 2020;16:e1009127.

16. Taylor K, Das S, Pearson M, Kozubek J, Pawlowski M, Jensen CE, Skowron Z, Møller GL, Strivens M, Gardner S. Analysis of Genetic Host Response Risk Factors in Severe COVID-19 Patients. medRxiv 2020;

17. Olzmann JA, Carvalho P. Dynamics and functions of lipid droplets. Nat Rev Mol Cell Biol 2018;1.

18. Hatters DM, Peters-Libeu CA, Weisgraber KH. Apolipoprotein E structure: insights into function. Trends Biochem Sci 2006;31:445–454.

19. Sturley SL, Hussain MM. Lipid droplet formation on opposing sides of the endoplasmic reticulum. J Lipid Res 2012;53:1800–1810.

20. Chorlay A, Monticelli L, Ferreira JV, M'barek KB, Ajjaji D, Wang S, Johnson E, Beck R, Omrane M, Beller M, Carvalho P, Thiam AR. Membrane Asymmetry Imposes Directionality on Lipid Droplet Emergence from the ER. Dev Cell [Internet] 2019 [cited 2019 May 31];0. Available from: https://www.cell.com/developmental-cell/abstract/S1534-5807(19)30374-0

21. Sui X, Wang K, Gluchowski NL, Elliott SD, Liao M, Walther TC, Farese RV. Structure and catalytic mechanism of a human triacylglycerol-synthesis enzyme. Nature 2020;1–6.

22. Santinho A, Salo VT, Chorlay A, Li S, Zhou X, Omrane M, Ikonen E, Thiam AR. Membrane Curvature Catalyzes Lipid Droplet Assembly. Curr Biol 2020;30:2481-2494.e6.

23. Wilfling F, Thiam AR, Olarte M-J, Wang J, Beck R, Gould TJ, Allgeyer ES, Pincet F, Bewersdorf J, Farese Jr RV. Arf1/COPI machinery acts directly on lipid droplets and enables their connection to the ER for protein targeting. Elife 2014;3:e01607.

24. Thiam AR, Ikonen E. Lipid Droplet Nucleation. Trends Cell Biol 2020;

25. Salo VT, Ikonen E. Moving out but keeping in touch: contacts between endoplasmic reticulum and lipid droplets. Curr Opin Cell Biol 2019;57:64–70.

26. Xu D, Li Y, Wu L, Li Y, Zhao D, Yu J, Huang T, Ferguson C, Parton RG, Yang H. Rab18 promotes lipid droplet (LD) growth by tethering the ER to LDs through SNARE and NRZ interactions. J Cell Biol 2018;217:975–995.

27. Thiam AR, Antonny B, Wang J, Delacotte J, Wilfling F, Walther TC, Beck R, Rothman JE, Pincet F. COPI buds 60-nm lipid droplets from reconstituted water–phospholipid–triacylglyceride interfaces, suggesting a tension clamp function. Proc Natl Acad Sci 2013;110:13244–13249.

28. Schuldiner M, Bohnert M. A different kind of love–lipid droplet contact sites. Biochim Biophys Acta BBA-Mol Cell Biol Lipids 2017;1862:1188–1196.

584 29. Jacquier N, Choudhary V, Mari M, Toulmay A, Reggiori F, Schneiter R. Lipid droplets are
585 functionally connected to the endoplasmic reticulum in Saccharomyces cerevisiae. J
586 Cell Sci 2011;124:2424–2437.

587 30. Thiam AR, Farese Jr RV, Walther TC. The biophysics and cell biology of lipid droplets. Nat
588 Rev Mol Cell Biol 2013;14:775.

589 31. Chitraju C, Mejhert N, Haas JT, Diaz-Ramirez LG, Grueter CA, Imbriglio JE, Pinto S,
590 Koliwad SK, Walther TC, Farese Jr RV. Triglyceride synthesis by DGAT1 protects
591 adipocytes from lipid-induced ER stress during lipolysis. Cell Metab 2017;26:407–418.

592 32. Nguyen TB, Louie SM, Daniele JR, Tran Q, Dillin A, Zoncu R, Nomura DK, Olzmann JA.
593 DGAT1-dependent lipid droplet biogenesis protects mitochondrial function during
594 starvation-induced autophagy. Dev Cell 2017;42:9–21.

595 33. Rambold AS, Cohen S, Lippincott-Schwartz J. Fatty acid trafficking in starved cells:
596 regulation by lipid droplet lipolysis, autophagy, and mitochondrial fusion dynamics. Dev
597 Cell 2015;32:678–692.

598 34. Syed GH, Amako Y, Siddiqui A. Hepatitis C virus hijacks host lipid metabolism. Trends
599 Endocrinol Metab 2010;21:33–40.

600 35. Penin F, Dubuisson J, Rey FA, Moradpour D, Pawlotsky J-M. Structural biology of
601 hepatitis C virus. Hepatology 2004;39:5–19.

602 36. Bartenschlager R, Cosset F-L, Lohmann V. Hepatitis C virus replication cycle. J Hepatol
603 2010;53:583–585.

604 37. Shi ST, Polyak SJ, Tu H, Taylor DR, Gretch DR, Lai MM. Hepatitis C virus NS5A colocalizes
605 with the core protein on lipid droplets and interacts with apolipoproteins. Virology
606 2002;292:198–210.

607 38. Shavinskaya A, Boulant S, Penin F, McLauchlan J, Bartenschlager R. The lipid droplet
608 binding domain of hepatitis C virus core protein is a major determinant for efficient
609 virus assembly. J Biol Chem 2007;282:37158–37169.

610 39. Boulant S, Montserret R, Hope RG, Ratinier M, Targett-Adams P, Lavergne J-P, Penin F,
611 McLauchlan J. Structural determinants that target the hepatitis C virus core protein to
612 lipid droplets. J Biol Chem 2006;281:22236–22247.

613 40. Boulant S, Targett-Adams P, McLauchlan J. Disrupting the association of hepatitis C virus
614 core protein with lipid droplets correlates with a loss in production of infectious virus. J
615 Gen Virol 2007;88:2204–2213.

616 41. Boyer A, Dumans A, Beaumont E, Etienne L, Roingeard P, Meunier J-C. The association of
617 hepatitis C virus glycoproteins with apolipoproteins E and B early in assembly is
618 conserved in lipoviral particles. J Biol Chem 2014;289:18904–18913.

42. Boulant S, Vanbelle C, Ebel C, Penin F, Lavergne J-P. Hepatitis C Virus Core Protein Is a Dimeric Alpha-Helical Protein Exhibiting Membrane Protein Features. J Virol 2005;79:11353–11365.

43. Moradpour D, Penin F, Rice CM. Replication of hepatitis C virus. Nat Rev Microbiol 2007;5:453–463.

44. Lindenbach BD, Rice CM. The ins and outs of hepatitis C virus entry and assembly. Nat Rev Microbiol 2013;11:688–700.

45. Counihan NA, Rawlinson SM, Lindenbach BD. Trafficking of hepatitis C virus core protein during virus particle assembly. PLoS Pathog 2011;7:e1002302.

46. Boson B, Granio O, Bartenschlager R, Cosset F-L. A concerted action of hepatitis C virus p7 and nonstructural protein 2 regulates core localization at the endoplasmic reticulum and virus assembly. PLoS Pathog 2011;7:e1002144.

47. Moriishi K, Okabayashi T, Nakai K, Moriya K, Koike K, Murata S, Chiba T, Tanaka K, Suzuki R, Suzuki T. Proteasome activator PA28γ-dependent nuclear retention and degradation of hepatitis C virus core protein. J Virol 2003;77:10237–10249.

48. Suzuki R, Matsuura Y, Suzuki T, Ando A, Chiba J, Harada S, Saito I, Miyamura T. Nuclear localization of the truncated hepatitis C virus core protein with its hydrophobic C terminus deleted. J Gen Virol 1995;76:53–61.

49. King C, Sengupta P, Seo AY, Lippincott-Schwartz J. ER membranes exhibit phase behavior at sites of organelle contact. Proc Natl Acad Sci 2020;

50. Jaiswal A, Hoerth CH, Pereira AMZ, Lorenz H. Improved spatial resolution by induced live cell and organelle swelling in hypotonic solutions. Sci Rep 2019;9:1–13.

51. Ajjaji D, Ben M'barek K, Mimmack ML, England C, Herscovitz H, Dong L, Kay RG, Patel S, Saudek V, Small DM. Dual binding motifs underpin the hierarchical association of perilipins1–3 with lipid droplets. Mol Biol Cell 2019;30:703–716.

52. Prévost C, Sharp ME, Kory N, Lin Q, Voth GA, Farese Jr RV, Walther TC. Mechanism and determinants of amphipathic helix-containing protein targeting to lipid droplets. Dev Cell 2018;44:73–86.

53. Chorlay A, Thiam AR. Neutral lipids regulate amphipathic helix affinity for model lipid droplets. J Cell Biol 2020;219.

54. Dhiman R, Caesar S, Thiam AR, Schrul B. Mechanisms of protein targeting to lipid droplets: A unified cell biological and biophysical perspective. In: Seminars in Cell & Developmental Biology. Elsevier; 2020.

55. Kory N, Thiam A-R, Farese Jr RV, Walther TC. Protein crowding is a determinant of lipid droplet protein composition. Dev Cell 2015;34:351–363.

654 56. Itabe H, Yamaguchi T, Nimura S, Sasabe N. Perilipins: a diversity of intracellular lipid
655 droplet proteins. Lipids Health Dis 2017;16:83.

656 57. Soni KG, Mardones GA, Sougrat R, Smirnova E, Jackson CL, Bonifacino JS. Coatomer-
657 dependent protein delivery to lipid droplets. J Cell Sci 2009;122:1834–1841.

658 58. Beller M, Sztalryd C, Southall N, Bell M, Jäckle H, Auld DS, Oliver B. COPI complex is a
659 regulator of lipid homeostasis. PLoS Biol 2008;6:e292.

660 59. Thiam AR, Dugail I. Lipid droplet–membrane contact sites–from protein binding to
661 function. J Cell Sci 2019;132:jcs230169.

662 60. Ohsaki Y, Cheng J, Suzuki M, Fujita A, Fujimoto T. Lipid droplets are arrested in the ER
663 membrane by tight binding of lipidated apolipoprotein B-100. J Cell Sci 2008;121:2415–
664 2422.

665 61. Tai AW, Benita Y, Peng LF, Kim S-S, Sakamoto N, Xavier RJ, Chung RT. A functional
666 genomic screen identifies cellular cofactors of hepatitis C virus replication. Cell Host
667 Microbe 2009;5:298–307.

668 62. Adeyo O, Horn PJ, Lee S, Binns DD, Chandrahas A, Chapman KD, Goodman JM. The yeast
669 lipin orthologue Pah1p is important for biogenesis of lipid droplets. J Cell Biol
670 2011;192:1043–1055.

671 63. Wang S, Idrissi F-Z, Hermansson M, Grippa A, Ejsing CS, Carvalho P. Seipin and the
672 membrane-shaping protein Pex30 cooperate in organelle budding from the
673 endoplasmic reticulum. Nat Commun 2018;9:2939.

674 64. Chorlay A, Thiam AR. An asymmetry in monolayer tension regulates lipid droplet budding
675 direction. Biophys J 2018;114:631–640.

676 65. Chorlay A, Santinho A, Thiam AR. Making Droplet-Embedded Vesicles to Model Cellular
677 Lipid Droplets. STAR Protoc 2020;100116.

678 66. Caillon L, Nieto V, Gehan P, Omrane M, Rodriguez N, Monticelli L, Thiam AR.
679 Triacylglycerols sequester monotopic membrane proteins to lipid droplets. Nat
680 Commun 2020;11:1–12.

681 67. Ben M'barek K, Ajjaji D, Chorlay A, Vanni S, Forêt L, Thiam AR. ER Membrane
682 Phospholipids and Surface Tension Control Cellular Lipid Droplet Formation. Dev Cell
683 2017;41:591-604.e7.

684 68. Santinho A, Chorlay A, Foret L, Thiam AR. Fat Inclusions Strongly Alter Membrane
685 Mechanics. Biophys J 2021;

686 69. Chang K-S, Jiang J, Cai Z, Luo G. Human apolipoprotein e is required for infectivity and
687 production of hepatitis C virus in cell culture. J Virol 2007;81:13783–13793.

688 70. Small DM, Wang L, Mitsche MA. The adsorption of biological peptides and proteins at
689 the oil/water interface. A potentially important but largely unexplored field. J Lipid Res
690 2009;50:S329–S334.

691 71. Skinner JR, Shew TM, Schwartz DM, Tzekov A, Lepus CM, Abumrad NA, Wolins NE.
692 Diacylglycerol enrichment of endoplasmic reticulum or lipid droplets recruits perilipin
693 3/TIP47 during lipid storage and mobilization. J Biol Chem 2009;284:30941–30948.

694 72. Lee J-Y, Cortese M, Haselmann U, Tabata K, Romero-Brey I, Funaya C, Schieber NL, Qiang
695 Y, Bartenschlager M, Kallis S. Spatiotemporal coupling of the hepatitis C virus
696 replication cycle by creating a lipid droplet-proximal membranous replication
697 compartment. Cell Rep 2019;27:3602–3617.

698 73. Bartenschlager R, Penin F, Lohmann V, André P. Assembly of infectious hepatitis C virus
699 particles. Trends Microbiol 2011;19:95–103.

700 74. Boson B, Denolly S, Turlure F, Chamot C, Dreux M, Cosset F-L. Daclatasvir prevents
701 hepatitis C virus infectivity by blocking transfer of the viral genome to assembly sites.
702 Gastroenterology 2017;152:895–907.

703 75. Markgraf DF, Klemm RW, Junker M, Hannibal-Bach HK, Ejsing CS, Rapoport TA. An ER
704 protein functionally couples neutral lipid metabolism on lipid droplets to membrane
705 lipid synthesis in the ER. Cell Rep 2014;6:44–55.

706 76. Salo VT, Li S, Vihinen H, Hölttä-Vuori M, Szkalisity A, Horvath P, Belevich I, Peränen J,
707 Thiele C, Somerharju P. Seipin facilitates triglyceride flow to lipid droplet and
708 counteracts droplet ripening via endoplasmic reticulum contact. Dev Cell 2019;50:478–
709 493.

710 77. Herker E, Harris C, Hernandez C, Carpentier A, Kaehlcke K, Rosenberg AR, Farese RV, Ott
711 M. Efficient hepatitis C virus particle formation requires diacylglycerol acyltransferase-
712 1. Nat Med 2010;16:1295–1298.

713 78. Boulant S, Douglas MW, Moody L, Budkowska A, Targett-Adams P, McLauchlan J.
714 Hepatitis C virus core protein induces lipid droplet redistribution in a microtubule-and
715 dynein-dependent manner. Traffic 2008;9:1268–1282.

716 79. Thiam AR, Beller M. The why, when and how of lipid droplet diversity. J Cell Sci
717 2017;130:315–324.

718 80. Herms A, Bosch M, Reddy BJ, Schieber NL, Fajardo A, Rupérez C, Fernández-Vidal A,
719 Ferguson C, Rentero C, Tebar F. AMPK activation promotes lipid droplet dispersion on
720 detyrosinated microtubules to increase mitochondrial fatty acid oxidation. Nat
721 Commun 2015;6:1–14.

722 81. Camus G, Schweiger M, Herker E, Harris C, Kondratowicz AS, Tsou C-L, Farese RV, Herath
723 K, Previs SF, Roddy TP, Pinto S, Zechner R, Ott M. The hepatitis C virus core protein
724 inhibits adipose triglyceride lipase (ATGL)-mediated lipid mobilization and enhances the

ATGL interaction with comparative gene identification 58 (CGI-58) and lipid droplets. J Biol Chem 2014;289:35770–35780.

82. Dansako H, Hiramoto H, Ikeda M, Wakita T, Kato N. Rab18 is required for viral assembly of hepatitis C virus through trafficking of the core protein to lipid droplets. Virology 2014;462:166–174.

83. Vieyres G, Reichert I, Carpentier A, Vondran FWR, Pietschmann T. The ATGL lipase cooperates with ABHD5 to mobilize lipids for hepatitis C virus assembly. PLOS Pathog 2020;16:e1008554.

84. Iglesias NG, Mondotte JA, Byk LA, De Maio FA, Samsa MM, Alvarez C, Gamarnik AV. Dengue virus uses a non-canonical function of the host GBF1-Arf-COPI system for capsid protein accumulation on lipid droplets. Traffic 2015;16:962–977.

85. Omrane M, Camara AS, Taveneau C, Benzoubir N, Tubiana T, Yu J, Guérois R, Samuel D, Goud B, Poüs C. Septin 9 has two polybasic domains critical to septin filament assembly and golgi integrity. Iscience 2019;13:138–153.

86. Pietschmann T, Kaul A, Koutsoudakis G, Shavinskaya A, Kallis S, Steinmann E, Abid K, Negro F, Dreux M, Cosset F-L, Bartenschlager R. Construction and characterization of infectious intragenotypic and intergenotypic hepatitis C virus chimeras. Proc Natl Acad Sci U S A 2006;103:7408–7413.

Figure 1: Core/D2 binding to the ER bilayer vs. LDs

(A) Illustration of immature Core anchorage to the ER bilayer by its D3 transmembrane domain. Cleavage at D3 releases mature Core. (B) HeliQuest Representation of the two amphipathic helices (AHs) of D2 linked by a hydrophobic loop. (C) Co-expression of mCherry-sec61ß with Core, immunolabeled by an Atto488 Antibody in Huh7 cells. Scale bar, 10µm. (D) (left)Expression of JFH1-Core leads to Core binding to LDs, on the left. (right) Overexpressed JFH1-D1D2 localizes to the nucleus. Scale bar, 10 µm. (E) Co-expression of mCherry-sec61ß with eGFP-D2 in Huh7 cells. Right panel: quantification of the signal of each protein by the LD/ER signal ratio, n=10 cells from 2 independent experiments. Scale bar, 10µm. (F) Principle for the generation of giant intracellular ER vesicles (GERVs) by submitting a Cos7 cell to a hypotonic medium. (G) GERVs in Huh7 cell transfected do not recruit eGFP-D2. GERVs are indicated by the luminal ER protein KDEL tagged with mRFP. Scale bar, 10 µm. (H) eGFP-Plin1 binds to GERVs in Cos7. GERVs are indicated by the luminal ER protein KDEL tagged with mRFP. Scale bar, 10 µm.

Figure 2: D2 better folds and associates with phospholipid artificial LDs.

(A) Triolein droplets and giant unilamellar vesicles (GUVs) are injected into the same observation chamber and eGFP-D2 was added. D2 bound to the triolein droplets (top) and not to the GUVs (bottom) of the chamber are shown. Scale bar is 40µm for the droplet panel, and 10µm for the GUV panel. (B) Rhodamine-N55A-AH is bound to the droplets and bilayers of the system. (C) Quantification of D2 and NS5A-AH signals on droplets and GUVs, n>3. (D) Representative FRAP analysis of eGFP-D2 on artificial triolein droplets, n>3, Scale bar, 20µm. (E) Circular dichroism (CD) spectrum of D2 in buffer (green), in the presence of artificial triolein LDs covered by dioleoyl phosphatidylcholine (PC). In blue, the spectrum of D2 in buffer alone. The two negative peaks at 210 and 230 nm are indicative of alpha-helices. (F) D2 CD spectrum in the presence of sonicated liposomes in green. (G) Schematic illustration of generated triolein droplets covered by different PC levels reported by Rhodamine-PE (Rho-PE) signal. (H) D2 bound to LDs with poor in Rho-PE. n>3, scale bar is 20 µm. (I) eGFP-D2 signal as a function of the relative density of phospholipids indicated by Rho-PE signal; 10 images analyzed from triplicates.

Figure 3: Protein crowding modulates the binding of D2 to LDs.

(A) Co-expression of eGFP-D2 with mCherry-perilipins 1-3 (Plin1-3) in Huh7.5 cells. D2 displaces Plin3, co-exists with Plin2, and is displaced by Plin1. Scale bar, 10 µm. Arrowheads indicate nuclear lipid droplets. (B) Quantification of the relative bound fraction of Plins and D2 on LDs, n=5, with a dozen cells analyzed for each condition. (C) Schematic illustration of the binding level of D2 in the presence of Plins. (D) Two examples of FRAP experiments of eGFP-D2 on LDs in Huh7.5. Insets correspond to the bleached regions and are shown before, during, and after bleaching. FRAP quantifications are on the right panel. Scale bar, 10 µm. (E) Characteristic recovery rates from 23 FRAP experiments are classified into three categories: inferior to 5sec, superior to 20sec, and between 5 and 20sec. The majority presents a characteristic recovery rate between 5 and 20sec. (F) FRAP of eGFP-D2 on different LDs within the same Huh7.5 cell. Different recovery kinetics are observed. Scale bar, 10µm.

Figure 4: Arf1/COPI regulates Core localization and infection.

(A) Immunofluorescence imaging of Core expressed in Huh7 in the presence or absence of Brefeldin A (BFA). LDs are marked by LipidTox. Yellow arrows indicate unbound LDs, and white arrows show LD with a partial core signal, n=10. Scale bar, 5 µm. (B) Histogram quantifying the frequency of the nuclear

localization phenotype with or without BFA. (C) Quantification of the impact of BFA treatment on Core localization per LD size classified into three categories: inferior to 1µm, superior to 2 µm, and between 1 and 2 µm. LDs inferior to 2 µm are more affected in BFA conditions. (D) expression of eGFP-D2 in Huh7 treated or not with BFA. Yellow arrows indicate Core-negative LDs, and the white arrows show LDs partially bound by D2, or cytosolic aggregates, n=10. Scale bar, 10 µm. (E) expression of Core in Huh7 previously treated with two different siRNAs against ßCOP. Core is revealed by immunofluorescence, n=3. Scale bar, 5 µm. (F) Quantification of the impact of the siRNA treatment on Core localization depending on LD size. (G) Schematic illustration of the complete HCV infection protocol on 24h in Huh7 in the presence or absence of BFA. (H) Images of cells infected with HCV. The left panel shows the Huh7 cells infected with HCV without BFA. Core is immunolabelled, visible on magenta on LDs and in puncta. The right panel shows cells treated with BFA. Core's signal is drastically diminished on LDs. Scale bar, 10µm. (I) Quantification of the intracellular and extracellular infectious particles, with or without BFA treatment, in OA induction. Condition +OA and -BFA is the same as in C. The minimum detection limit for infectious particles is 50 and 10 FFU / mL, respectively, for intra- and extra-cellular media. The particles' formation is affected in BFA conditions.

Figure 5: Impact of neutral lipid synthesis on the ER localization of D2.

(A) A swollen Cos7 is incubated with OA and BODIPY-C12, to induce the synthesis of fluorescent triacylglycerol (TG), and LipidTox. The presence of TG in the bilayer of GERVs favors the recruitment of eGFP-D2: eGFP-D2, Bodipy-C12 and LipidTox signals are shown. (B) Same experiment as in (A) with cells transfected with BFP-ER. (C) The recruitment of D2 to GERVs increases with the LipidTox signal in OA induction cells. (D) Illustration of D2 recruitment to bilayers lacking of containing TG. (E) D2 binding to GERVs is decreased by the presence of DGAT inhibitors under OA addition. (F) Quantification of the recruitment level of D2 to GERVs fed with OA. (G) FRAP experiment of eGFP-D2 on a GERV, in the OA loaded condition. (H) Comparison of recovery rates between LDs and GERVs. (I) GERVs are generated from Cos7 cells that expressed mCherry-Sec61 and have been incubated with OA. eGFP-D2 failed to efficiently bind to the GERVs. (J) The recruitment level of D2 to GERVs increased with decreased Sec61 signal.

Figure 6: Triacylglycerols are determinant to D2 localization in vitro.

(A) (top) Principle of the droplet-embedded vesicles (DEV) preparation before eGFP-D2 is injected into the system. The Rhod-PE signal reports for phospholipids. (bottom) eGFP-D2 binds efficiently only to the droplets and not to the bilayer of the DEV. n>5. Scale bar, 20 µm. Quantification of the D2 signal on the droplet vs. the bilayer region of the DEV over time is shown on the right panel. (B) Schematic illustration of a DEV and its bilayer region. Water addition stretches the bilayer due to swelling, delivering more TG from the droplet to the bilayer. During swelling, D2 signal in the bilayer increases. The increase of the bilayer area is shown on the top right (in red). R represents the DEV radius at a given time and R(0) is the initial radius. Quantification of D2 localization to the bilayer is shown on the bottom right panel (in black), n=3. Scale bar, 20 µm. (C) The swelling experiment by adding water is done on a bare GUV and eGFP-D2 does not bind. The increase of the bilayer area is shown on the top right. R represents the DEV radius at each time and R(0) represents the initial radius. Quantification of D2 localization to the bilayer is shown on the bottom right panel, n=3. Scale bar, 20 µm. (D) Sequence alignment of Core-D2 and apoE shows a highly conserved region corresponding to the apoE reported lipid-binding region. (E) Schematic illustration of an oil droplet, before and after protein addition, and the associated decrease in surface tension measured by a tensiometer. ST_{in} and ST_{eq} are, respectively,

the initial surface tension of the bare oil/water interface and the equilibrium tension after proteins adsorb to the interface. (F) Evolution of the surface tension over time in the presence of D2 for triolein/water and squalene/water interfaces. (G) The relative surface tension decrease induced by D2 and apoE adsorption to the triolein/water vs. squalene/water interfaces are shown.

Figure 7: Proposed model for Core cellular trafficking and conditions favorable for viral assemblies. (A) In the presence of an LD connected to the ER, Core can either fold to the LD and move back to the ER membrane with TG molecules or bind directly to TG in the ER. A fraction of the protein is degraded in the nucleus. (B) In the absence of LDs, Core can bind to the ER membrane, and the assembly of virions can occur if TG is infused in the ER bilayer. A fraction of the protein is still degraded in the nucleus. (C) In the presence of an LD physically disconnected from the ER, Core can still bind to the LD, but the assembly of virions is decreased because of the absence of TG in the ER bilayer. Here, most Core will proteins will end up being degraded in the nucleus. (D) In the absence of TG, Core is majorly degraded, in the nucleus.

Figure S1: Characterization of Core/D2 cellular and in vitro localization

(A) Expression of J6-Core leads to Core binding to LDs, the top panel. In J6-D1D2 expression in MG132-treated cells, bottom panel, Core shows nuclear localization. Scale bar, 10 µm. (B) Other examples of eGFP-D2 expression in Huh7 cells showing no noticeable ER membrane localization. Scale bar, 10 µm. (C) Co-expression of mCherry-sec61ß with eGFP-D2 in Hela cells reveals that D2 does not bind to the ER. LDs are marked by LipidTox, n=2. Scale bar, 10 µm. (D) Expression of eGFP-D2 in HeLa cells where ER is represented by a lumen ER protein in BFP. Before swelling on the top and after swelling at the bottom. (E) Expression of eGFP-Plin1 in HeLa cell where ER is represented by a lumen ER protein in BFP. Before swelling on the top and after swelling at the bottom. Scale bar, 5 µm.

Figure S2:

(A) Helical wheel representation of the AHs of D2 (left) and NS5A (right). Red-encircled amino acids are bulky hydrophobic residues. (B) Circular dichroism (CD) spectrum of D2 in buffer (blue), in the presence of artificial LDs, made with dioleoyl phosphatidylcholine (PC) at 1% (Left) or 0.1% (Right). The two negative peaks at 210 and 230 nm are indicative of alpha-helices. (C) D2 CD spectrum in the presence of small sonicated liposomes in 50 nm diameter range (Left) and larger liposomes formed (average diameter of 500 nm of average diameter). (D) FRAP of eGFP-D2 on a triolein-in-buffer droplet shows ultra-slow recovery. The arrow depicts the bleached droplet. (E) Different phenotypes of D2 in the presence of LD with different PC densities, shown separately. D2 signal colocalized on droplets where Rhod-PE signal is weaker. n>3, scale bar is 20 µm. (F) Another example of D2 phenotype in the presence of a droplet mix of different PC densities.

Figure S3: Characterization of D2/Core binding depending LD surface cover composition

(A) Expression of mCherry-perilipins 1-3 (Plin1-3) in Huh7.5 cells. All proteins bind to LDs. (B) Schematic illustration of the competition between proteins (D2 in green and Plin1 in red) at the interface of a water-in-oil shrinking droplet. (C) Representative images of the fall off of eGFP-D2 from the water/oil interface during shrinkage, while mCherry-Plin1 remained stably bound. The relative fluorescence intensity profiles in the shown plane are embedded in the images. On right panel, the average surface / volume signal during compression is plotted over the compression factor, (r_0^2 (time=0) / r^2 (at each time point). The experiment has been repeated three times. (D) Images of co-expression of Core and GFP-Plin1. Scale bar, 10 µm. (E) Series of FRAP experiments of eGFP-D2 on LDs in Huh7.5. These 23 FRAPs are regrouped in Figure 3E. (F) Expressed pTG1-eGFP-(GGGGS)-D2 (i.e., 1 linker between eGFP and D2) and pTG2-eGFP-$(GGGGS)_2$-D2 (i.e., 2 linkers between eGFP and D2) in Huh7.5 cells bound to LDs. Scale bar, 10 µm. (G) FRAP in Huh7.5 of pTG1-eGFP-(GGGGS)-D2 and pTG2-eGFP-$(GGGGS)_2$-D2 on LDs. Scale bar, 10 µm.

Figure S4: Arf1/COPI impact on Core localization.

(A) Additional examples of the two observed phenotypes of Core in Huh7 cells treated with BFA. White and yellow arrows respectively indicate LDs having partial or no Core signal. Scale bar, 10 µm. (B) Quantification of Core localization depending on LDs' size, with or without BFA. For each LD size range, hundreds of LDs are quantified for the different Core localization phenotypes. (C) FRAP experiment of D2 forming an arc signal around LDs in BFA condition. Scale bar, 5 µm. (D) Other examples of the localization of Core in cells treated with a ßCOP siRNA. Scale bar, 5µm. Quantification of the Core localization depending on LD size in the control and the siRNA treatments are shown on right. Hundreds of LDs are quantified from over twenty cells. (E) Immunoblotting against COPI, Core, ADRP, and GAPDH in the fractions of post-nuclear supernatant (PNS) and LDs, treated or not with the ßCOP siRNA. (F) Core LD phenotypes in the presence of ßCOP siRNAs. Two siRNAs and a mix of both are

tested. For these experiments, the Golgi is labeled with KDE-GFP. The Golgi appears more fragmented in the presence of the siRNAs compared to the control cells, where KDE-GFP signal is more compact and perinuclear. The Western Blot indicating the efficiency of the siRNA is shown under each treated condition. Scale bar, 5 µm. (G) Schematic illustration of the complete HCV infection protocol with or without induction of LDs, over 24 hours. (H) Images of Core in cells infected with the Jc1 strain, treated (bottom) or not (top) with OA. Scale bar, 10 µm. (I) Images of cells infected with HCV Jc1 and transfected with Plin1, 2, or 3. Plin and Core signals are shown. Scale bar, 5 µm. (J) Quantification of the intracellular and extracellular infectious particles, with or without OA incubation. (K) 32 h protocol diagram, with BFA washing at 24 h post-infection. (L) Quantification of the infectious particles before adding BFA and after adding then washing BFA at 1 µg / mL.

Figure S5: D2 binding to the ER

(A) eGFP-D2 does not bind to the intracellular GERVs, labeled by mRFP-KDEL, in swollen Cos7. On the left, control condition of Cos7 before swelling and under the co-expression of eGFP-D2 and mRFP-KDEL. In the middle panel, D2 is absent from the GERV in swelling condition and cytosolic. In the right panel, under swelling and OA addition, D2 localizes on intracellular GERVs. (B) Control, swelling, and swelling with OA addition conditions. D2 is located to OA-rich intracellular GERVs. (C) (top) Image of D2 biding to LipidTox-rich GERVs. D2 binding level to GERVs increases with the LipidTox signal. (D) Protocol illustrating the use of DGAT1/2 inhibitors (iDGAT1/2) in Cos7 cells. Inhibitors are added, then eGFP-D2 is transfected to cells. After 24h of transfection, live imaging is performed and the cell are swollen, with replacing the cell culture medium with the hypotonic medium containing also the inhibitors. The last step is OA addition. (E) In the presence of DGAT inhibitors, before swelling, D2 is cytosolic; in the swollen condition, D2 is absent from GERVs. In swollen conditions, with OA addition, D2 is absent from GERVs. (F) Another protocol where the DGATi are added in the meantime of OA addition. (G) The same results are obtained with the precedent protocol in Figure S5D-E. (H) Other FRAP experiments of D2 on GERVs. (I) The recruitment level of D2 to GERVs increases with LipidTox signal (in green) and decreases with mCherry-Sec61 signal (in magenta).

Figure S6: Comparisons between D2 and apoE.

(A) Two examples of DEVs showing the binding of eGFP-D2 mostly to the droplet. (B) Rhod-NS5A-AH binds to both the droplet and the bilayer region of the DEV. (C) Display of the crystalized structure of apoE (PDB NCBI Reference Sequence: NP_001289617.1). (D) Sequence alignment of apoE with D1 Core. (E) Phylogenetic tree comparing sequence alignments of D2, Plins 1-3, apoE, apoC1, DENV NS1, and Envelope glycoprotein ASFV. In contrast to perilipins, D2 is close to apoE, apoC1, and the non-structural protein 1 of the Dengue virus. (F) Evolution of the surface tension over time in the presence of apoE for triolein/water and squalene/water interfaces.

Movie: Example of a FRAP experiment carried on in a cell where two regions of LDs are simultaneously bleached. eGFP-D2 showed a differential recovery rate between the LD subpopulations.

Material & methods

Plasmids and peptides. The plasmids phCMV-core JFH1, pTG-eGFP-D2 JFH1, and mCherry-NS5A that express Core, D2, and NS5A, respectively, were kindly provided by our collaborator Bertrand Boson (ENS Lyon). The linkers $(GGGGS)_1$ or $(GGGGS)_2$ linkers were inserted between D2 and eGFP into pTG1-eGFP-D2 and pTG2-eGFP-D2, respectively, by directed mutagenesis with the following oligos: pTG1-FW 5'-AGG-GTC-TTC-CGG-ACT-CAG-ATC-TAA-C-3'; pTG1-RW 5'-CCG-CCA-CCC-TTG-TAC-AGC-TCG-TCC-ATG-3'; pTG2-FW 5'-GGT-GGC-GGA-GGA-TCT-TCC-GGA-CTC-AGA-TCT-AAC-3'; pTG2-RW 5'-AGA-TCC-TCC-GCC-ACC-CTT-GTA-CAG-CTC-GTC-CAT-G-3'. The plasmids that express PLIN peGFP-Plin 1-3, were kindly provided by the team of University of Cambridge Metabolic Research Laboratories. The human protein ApoE (Sigma-Aldrich). Peptide J6-D2 was obtained from François Penin and has the following sequence NLGKVIDTLTCGFADLMGYIPLVGAPLGGAARALAHGVRVLEDGVNYATGN. For comparison, the JFH1-D2 sequence is: NVGKVIDTLTCGFADLMGYIPVVGAPLSGAARAVAHGVRVLEDGVNYATGN.
To mark Golgi, we used the plasmid KDE-GFP (Dipeptidyl peptidase IV in which the extracellular domain had been replaced by the GFP sequence to restrict protein localization to the Golgi apparatus [85]), was kindly given by Professor Christian Poüs (Paris-Sud University, France).

Expression constructs. pFK-JFH1/J6/C-846_dg plasmid was kind gift from R. Bartenschlager [86]. phCMV-core JFH1 and phCMV-core J6 plasmids were previously described [46]. phCMV-core FP- JFH1 and phCMV-core CS- J6 were constructed by inserting a stop codon by mutagenesis after the amino acid 171 of the core protein in phCMV-core JFH1 and phCMV-core J6, respectively.

Production of the recombinant peptide eGFP-D2.

The eGFP-D2 DNA sequence was cloned into pET15b (Novagen, Merck) between NdeI/BamHI restriction sites. Induction of eGFP-D2 expression in BL21pLys (Invitrogen, Thermofischer) was done at +37°C for 3h, after addition of 0.5 mM IPTG (Sigma-Aldrich) at 0.5DO of growth in LB supplemented with 100µg/mL ampicillin. Bacterial were centrifuged at 5000g for 15min at 4°C. The pellet was resuspended in 35mL of 20mM phosphate buffer at pH = 7.4, supplemented with 500mM NaCl, 10% glycerol, 1mM PMSF and 50µg/mL lysozyme (Sigma-Aldrich, Merck) and submitted to French Press extraction at 1500 PSI (Thermofischer). After centrifugation of the crude lysate at 25000g, 4°C for 30min, the supernatant was filtered on 0.45µm, and 0.20µm cellulose membranes (Merck) before loading on 1mL HisTrap HP affinity column (Amersham, GE Healthcare) conditioned with extraction buffer. Protein eGFP-D2 was eluted with 250mM imidazole (Sigma-Aldrich) after linear gradient from 40mM to 1M imidazole in 15CV (Akta purifier Amersham, GE Healthcare). After analysis of 20µL of each fraction on Novex BisTris, 4-12% PAGE (Life Technologies Thermofischer) revealed with Coomassie blue (PageBlue, Thermofischer), fractions containing 33kDa proteins were pooled and dialyzed O/N at +4°C in 20mM phosphate buffer pH = 7.4 supplemented with 50mM NaCl, 10% glycerol. The dialyzed fractions were loaded on a MonoQ equilibrated with dialysis buffer (Amersham, GE Healthcare) and submitted to a linear gradient from 50mM to 1M NaCl for anionic exchange. The protein eGFP-D2 was eluted with 250mM NaCl, analyzed on PAGE, and quantified by spectrophotometry by measuring absorbance in UV (from 190nm to 340nm) and at 488nm. We obtained 1,5 mg of highly purified eGFP-D2 protein at 23 µM.

Antibody. Monoclonal antibodies (references 19D9D6, Bio-Merieux) of mice directed against Core HCV proteins (recognize the Core D1 domain) were used to detect the location of Core in the transfected cells. The secondary antibodies of donkey anti-mouse marked with the Alexa 555 anti Monoclonal antibodies 19D9D6 (provided by our employees of the ENS, Lyon, references A-31570, Invitrogen). These antibodies are used in immunofluorescence, diluted to 1/1000. For virology experiments: Mouse anti-core 19D9D6 (kind gift from C. Jolivet, bioMérieux, Lyon, France), Mowiol 40-88 (Fluka, Switzerland), Oleic Acid-Albumin and BFA (Sigma Aldrich, France), BODIPY 493/503, LipidTox Deep Red, Hoechst 33342 (Molecular Probes Europe BV, The Netherlands) and Gene Jammer (Agilent, United States) were used according to the manufacturer's instructions.

Cell Culture and reagents. Huh7, Huh7.5, and HeLa cells were maintained in Dulbecco's modified Eagle's medium (DMEM) supplemented with 10% heat-inactivated fetal bovine serum (Life Technologies), 4.5 gL^{-1} D-glucose, 0.1 gL^{-1} sodium pyruvate (Life Technologies), and 1% penicillin-streptomycin (Life Technologies). The cells were cultured at 37°C under a 5%CO2 atmosphere. HeLa (human cervical carcinoma obtained from the American Type Culture Collection) cells were maintained in DMEM supplemented with 10% (vol/vol) FBS, 2 mM l-glutamine, penicillin–streptomycin, 1% sodium pyruvate, and 1% nonessential amino acids. For virology experiments: Huh7.5 cells (king gift from C. Rice) were grown in Dulbecco's modified minimal essential medium (DMEM, Invitrogen, France) supplemented with 100U/ml of penicillin, 100µg/ml of streptomycin, and 10% fetal bovine serum.

Transfection and co-transfection. When indicated, Huh7 or HeLa cells (60–70% confluence) plated into a 35 mm cell-culture MatTek dishes (with a glass coverslip at the bottom), (MatTek Corp. Ashland, MA). were exposed for 1 h to 350 µM oleic acid (OA) coupled to bovine serum albumin (BSA) (1% vol/vol) to induce LD formation, and then cells were transfected with 3 µg of plasmid DNA/ml using Polyethylenimine HCl MAX (Polysciences) following the manufacturer's instructions. For coexpression competition experiments, mCherry- or GFP-tagged plasmid constructs in equal concentrations (1.5–2 µg for each one) were transfected into cells. Cells were imaged at 24 h after transfection. For virology experiments: HCV core or GFP-PLIN expression. HCV core or eGFP-PLIN expression plasmids were transiently expressed in Huh7.5 cells by transfection with GeneJammer transfection reagent according to the manufacturer's instructions. Briefly, $2.10e^5$ Huh7.5 cells seeded in 6-well plates were transfected with 2µg of DNA and 4µL of GeneJammer diluted in Optimem medium for 8h or 16h. The medium was then replaced by a fresh medium for HCV core expression studies or by a medium containing Jc1 at MOI=0.2 for eGFP-PLIN studies, and cells were then cultured for the indicated time.

HCVcc production and titration. HCVcc production procedures were described previously [86]. Supernatants infectivity titers were determined as focus-forming units (FFU/ml). Serial dilutions of supernatants were used to infect Huh7.5 cells, FFUs were determined 3 days post-infection by counting NS5A-immunostained foci. For determining intracellular infectivity, infected cells were washed with PBS and harvested after trypsin treatment and centrifuged for 4 min at 400xg. Cell pellets were suspended in medium and subjected to 4 cycles of freeze and thaw with liquid nitrogen. Serial dilutions of this cell lysate were then used for supernatants to determine the intracellular infectivity.

FRAP experiments. For FRAP experiments, we bleached the signal on a cluster of drops and monitored the increase of signal during recovery. The background signal, for example, from the cytosol, was removed from the recorded signal, which was at the end normalized by intrinsic bleaching of non-bleached areas. We next used GraphPad Prism to fit the FRAP recovery curves with a nonlinear regression and the exponential one-phase association model. The characteristic recovery time that corresponds to the time it takes for fluorescence intensity to reach half the maximum of the plateau level is obtained by the software.

Cellular Fractionation. For purification of LDs from cells expressing fluorescently tagged LD proteins, cells from five 150 cm dishes were harvested, washed once in ice-cold PBS, and lysed using a 30G needle in 1 ml Tris-EDTA (20-10 mM, respectively) buffer containing complete protease and phosphatase inhibitor tablets (ThermoFisher) at pH 7.5. For LD isolation, 1 ml of cell lysates was mixed with 1 ml of 60% sucrose in Tris-EDTA buffer supplemented with protease inhibitors, overlaid with 20, 10, and 0% buffered sucrose on top of one another in 5 ml Ultra-Clear centrifuge tubes (Beckman). Gradients were centrifuged for 16 h at 100,000 × *g* and 4°C, using an SW60 rotor in a Beckman L8-70 centrifuge, and 300 µl was collected from the top as the LD fraction.

Western Blot. The different purified cell fractions were migrated on a 10% SDS PAGE gel (cast in the laboratory), and the bands of the gel were electro-transferred onto a nitrocellulose membrane (Schleicher & Schuell). The membrane was then incubated with an anti-Core (MA1-080, ThermoFisher)/ ADRP (ab52355, Abcam) / COPI (ab2899, Abcam) / actin monoclonal antibody (sc-47778 HRP, SantaCruz), from Abcam, followed by incubation with HRP-conjugated secondary IgG and visualized by a Pierce ECL kit (Thermofisher).

Immuno-fluorescence (IF) and confocal microscopy imaging. Huh7 cells grown on 35 mm cell-culture MatTek dishes were transfected with Core plasmid. 24 h post-transfection, Cells were fixed with 4% formaldehyde for 15 min; this was followed by three washes in phosphate-buffered saline (PBS), then permeabilized with 0.3% Triton X-100 for 10min at room temperature. Fixed cells were then incubated for the night with anti-Core antibody diluted 1/1000 in 3% BSA/PBS, washed and stained for 1h with fluorescent secondary antibody (anti-Mouse AlexaFluor-555, Molecular Probes Europe BV, The Netherlands) in 3% BSA/PBS. LDs were stained with 10µg/mL BODIPY 493/503 or with LipidTox Deep Red according to the manufacturer's instructions. Cells were washed and mounted on microscope slides with ProLong Gold Antifade Mountant with 4',6-diamidino-2-phenylindole (Thermo Fisher Scientific), and the fluorescently tagged protein localization was determined using a Leica TCS SP8 confocal microscope with a 63× immersion oil objective (1.3 NA).
GFP fluorescence was excited at 488 nm, and emission was detected between 490 and 550 nm, while M-cherry–tagged protein fluorescence was excited at 588, and emission was detected between 600 and 650 nm. LDs were detected with either BODIPY 493/502 (excitation: 502 nm; emission: 515–560 nm) or LipidTox Deep Red (excitation: 558 nm; emission: 590–700 nm).
For virology experiment: Huh7.5 cells grown on uncoated 14mm-diameter glass coverslips were infected with HCVcc at MOI of 0.2. When stated, the viruses were removed 8h post-infection and replaced by media containing 1µg/mL of BFA or diluent (EtOH) for 24h. At indicated times post-infection, cells were washed with PBS, fixed with 3% paraformaldehyde

in PBS for 15min, quenched with 50mM NH_4Cl, and permeabilized with 0.1% Triton X-100 for 7min. Fixed cells were then incubated for 1h with anti-core antibody diluted 1/1000 in 1% BSA/PBS, washed and stained for 1h with fluorescent secondary antibody (anti-Mouse AlexaFluor-555, Molecular Probes Europe BV, The Netherlands) in 1% BSA/PBS. LDs were stained with 10µg/mL BODIPY 493/503 or with LipidTox Deep Red 1/200 according to the manufacturer's instructions. Cells were washed three times with PBS, stained for nuclei with Hoechst (Molecular Probes) for 5min when stated, washed, and mounted in Mowiol prior to image acquisition with LSM-710 confocal microscopes.

Interference RNA and inhibitor treatment. For COPI inhibition, Huh7 cells were grown on 35 mm cell-culture MatTek dishes and were treated with siRNA (Dharmacon) complexed with HiPerFect Transfection Reagent (Qiagen), according to the manufacturer's instructions for 24h. For siRNA experiment, two lots are used, Lot1 (Horizon, D-017940-04-0002), Lot2 Horizon, D-017940-03-0002). Then treated cells were incubated with OA and transfected with Core plasmid. 24 h post-transfection, cells were fixed, and IF protocol was applied. For Brefeldin A inhibition, it is added 4h post-transfection, and cells are imaged 20h after inhibition. For the DGAT1 (Sigma PF-04620110) and DGAT2 (Sigma PF-06424439) inhibitors used in Cos7, the dilution applied was 1/1000 for a final concentration of 3ug/mL. In the GERV protocol (Figure 5D, S5D-E), the inhibitors were added when the cell medium is replaced by a hypotonic medium, and/or just before cell transfection (Figure S5F-G).

Circular Dichroism CD. The CD spectra were obtained on a Joblin-Yvon CD6 device. The scan speed is set at 0.2 nm / s. The measurements were carried out in a quartz tank 1 mm in diameter. A blank (buffer solution) is made before each measurement and is subtracted from the protein spectra. For each measurement, three spectra were recorded to increase the signal-to-noise ratio. The final concentrations of peptides used are between 90 and 150 µM in 10 mM sodium phosphate buffer (pH 7.4) supplemented with 100 mM potassium chloride KCl and 2 mM MgCl 2 (buffer called PKM). The results are presented in standardized Δε values on the basis of the mass of an amino acid residue of 110 KDa using the formula: $\Delta\varepsilon = \Delta A / (l * C * n)$, with Δε which is the difference of molar extinction coefficient in $M^{-1}.cm^{-1}$, ΔA is the absorption difference, l is the optical path in cm, C is the molar concentration in mol / L and n is the number of residues of the analyzed peptide. The sensitivity of the dichrograph is $\delta(\Delta A) = 10^{-6}$.

Bioinformatics.

Heliquest was used for α-helix projections (www.heliquest.ipmc.cnrs.fr). Hydrophobic AAs are illustrated in yellow. For D2, we use the two amino-acids sequences NVGKVIDTLTCGFADLMGY and ARAVAHGVRVLEDGVNYATGN, which represent the two AHs of D2, respectively.

For data presented in Figure 6D and Figure S6D, EMBOSS Water pairwise sequence **local alignment tool**, https://www.ebi.ac.uk/Tools/psa/emboss_water/, was used to study the similarity between human APOE, APOC1, PLIN1-3, HCV JFH1 core, D1 and D2, Flavivirus Envelope glycoprotein (from African swine fever virus (ASFV) and Nonstructural protein NS1 (from Dengue virus (DENV).

Shrinking experiments. *In vitro* experiments were performed in HKM buffer: 50 mM HEPES, 120 mM potassium acetate, and 1 mM MgCl2 (in Milli-Q water) at pH 7.4. To create a buffer in oil drops, 4 µl of a buffer-diluted LD fraction was mixed with 40 µl of triolein vortexing.

About 100 drops were formed and imaged in the field of observation. For shrinking experiments, aqueous drops bounded by the proteins were imaged for 10–30 min on glass plates during water evaporation.

Giant Unilamellar Vesicles and Artificial Lipid Droplets Formation GUVs. GUVs were prepared by electroformation. Phospholipids and mixtures thereof in chloroform at 0.5 mM were dried on an indium tin oxide (ITO)-coated glass plate. The lipid film was desiccated for 1 h. The chamber was sealed with another ITO- coated glass plate. The lipids were then rehydrated with a sucrose solution (275 mOsm). Electroformation is done using 100 Hz AC voltage at 1.0 to 1.4 Vpp and maintained for at least 1 h. This low voltage was used to avoid hydrolysis of water and dissolution of titanium ions glass plate. GUVs were either stored in the chamber at 4°C overnight or directly collected with a Pasteur pipette.
To prepare the artificial lipid droplets (aLDs), 5 mL of the lipid oil solution was added to 45 mL of HKM buffer. The mixture was sonicated. The diameter of the resulting droplets is a few hundred nanometers.

Droplet-embedded vesicles' preparation: Unless mentioned, *in vitro* experiments were performed in the following HKM buffer: 50 mM Hepes, 120 mM Kacetate, and 1 mM MgCl2 (in Milli-Q water) at pH 7.4 and 275±15 mOsm. All **GUVs** were 70 % DOPC 29% Rhodamine-DOPE 1% (w/w) Rhodamine-DOPE. GUVs were prepared by electro-formation. Phospholipids and mixtures thereof in chloroform at 0.5 mM were dried on an indium tin oxide (ITO) coated glass plate. The lipid film was desiccated for 1 h. The chamber was sealed with another ITO coated glass plate. The lipids were then rehydrated with a sucrose solution (275+-15 mOsm). Electro-formation is performed using 100 Hz AC voltage at 1.0 to 1.4 Vpp and maintained for at least 1 h. This low voltage was used to avoid hydrolysis of water and dissolution of the titanium ions on the glass plate. GUVs were either stored in the chamber at 4°C overnight or directly collected with a Pasteur pipette. To prepare the aLDs, 5 μL of the oil was added to 45 μL of HKM buffer. The mixture was sonicated. The diameter of the resulting droplets is on the order of a few hundred nanometers. To make DEV, GUVs were then incubated with the aLDs for 5 min. The GUV-LD mixture was then placed on a glass coverslip pretreated with 10%(w/w) BSA and washed three times with buffer.

Giant ER vesicles' generation. For cell swelling experiments, Cos7 cells were first transfected for 24 h with the eGFP-D2 plasmid. The culture media was next replaced by a hypotonic culture media (DMEM: H2O, 1:20). The cells were then incubated at 37°C, 5% CO2 for 5 minutes, to induce ER-vesicles. For analyzing D2 localization, cells were imaged directly after swelling. The cells were next incubated with 400 μM OA conjugated to 1% (w/w) BSA in DMEM: H2O (1:20) media at 37°C to induce triacylglycerol (TG) synthesis. Then BODIPY-C12 558/568 was also added to OA (1:1000) to induce and visualize fluorescent TG localization. Z-stacks imaging of entire cells was done before and 15 min after OA administration. Z-stacks of the entire cell were imaged after swelling, before feeding, and 15 minutes after feeding. mCherry-KDEL and ER-BFP or mCherry-Sec61ß are used as a marker of ER lumen or ER membrane, respectively.

GUV Swelling experiments. MilliQ water was added to the bulk HKM buffer of the GUVs: 10 μL of MilliQ was added to the 100 μL of HKM buffer.

Interfacial tension measurements (γ)

We used an oil-drop tensiometer (Mitsche et al., 2010; Mitsche and Small, 2013; Meyers et al., 2013) designed by Teclis Instruments (Tassin, France) to measure the interfacial tension (γ) of lipid–water interfaces. All experiments were conducted at 25.0 ± 0.2°C in a thermostated system and repeated at least twice.

For the creation of TO–Water or squalene-Water interfaces (Mitsche and Small, 2011), TO or squalene Sq drops (5 µL) were formed at the tip of a J-needle submerged in 5 ml of bulk buffer. Their surface area was ∼30 mm2 (diameter = 3.1 mm). The buffer was 5 mM HKM (50 mM Hepes, 120 mM K acetate, and 1 mM $MgCl_2$ (in Milli-Q water)
at pH 7.4. The TO–W interface stabilized at γTO = 32.0 ± 1 mN/m. The Sq–W interface stabilized at γSq = 22.0 ± 1 mN/m.

Adsorption of proteins (i.e., D2, ApoE) to the interface decreases γ to a nearly constant value defined as equilibrium tension (γ_{eq}). D2 or ApoE peptide was added to the bulk phase to obtain final protein concentrations of 0.18 µM and 0.014 µM, respectively. As peptide adsorbed to TO–W and Sq–W interfaces, γ was monitored until it fell to an equilibrium value (γ_{eq}).

Relative tension decrease was defined as the difference in γ between a pure TO–W or Sq-W interface (γTO = 32.0 mN/M; γSQ= 22.0 mN/M) and the interface at the equilibrium with bound peptide (Relative tension decrease = $\gamma TO - \gamma_{eq})/\gamma TO$ and (Relative tension decrease = $\gamma SQ - \gamma_{eq})/\gamma SQ$.

Quantification and statistical analysis

Fluorescent signal quantification at LD or GUV surface

To quantify the recruitment of the fluorescent protein at the surface of LDs, we used the radial angle profile plugin of ImageJ software. This plugin measures the average signal intensity along the perimeter of concentric circles. It results in a plot of the intensity profile of a circular object for various positions relative to its center. We chose the maximum intensity profile as a measurement of recruited peptide density. The same method was used to quantify the phospholipid density covering droplets. For the competition experiment, protein concentrations on LDs were derived from the mean fluorescence measured on LDs in each channel (Plins vs. D2, Figure 3); each experimental point corresponds to the average of the signal on 10–20 LDs. Values from 15–20 cells were combined, and the SD was calculated for statistical analysis. Values from 15–20 cells were combined, and the SD was calculated for statistical analysis.

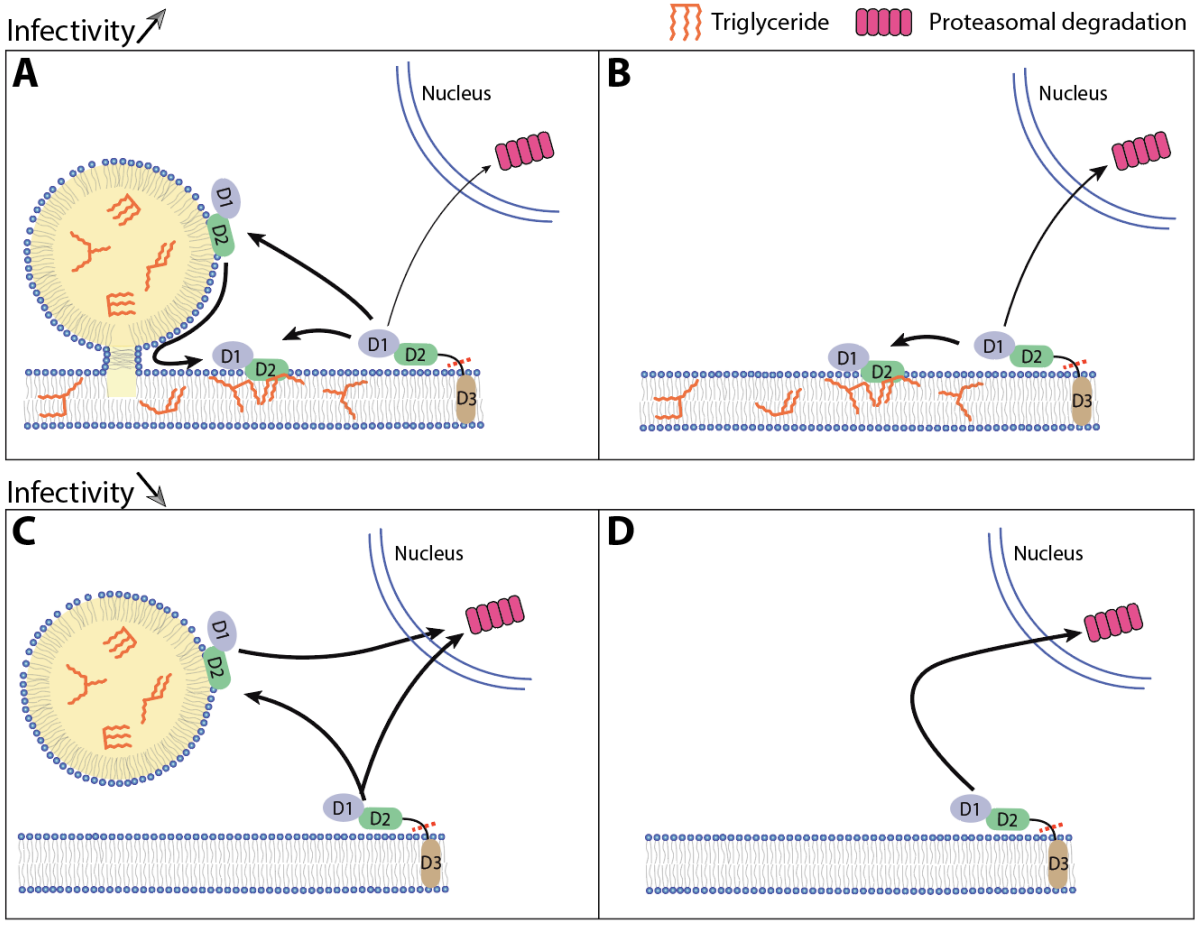

1214

Figure 7

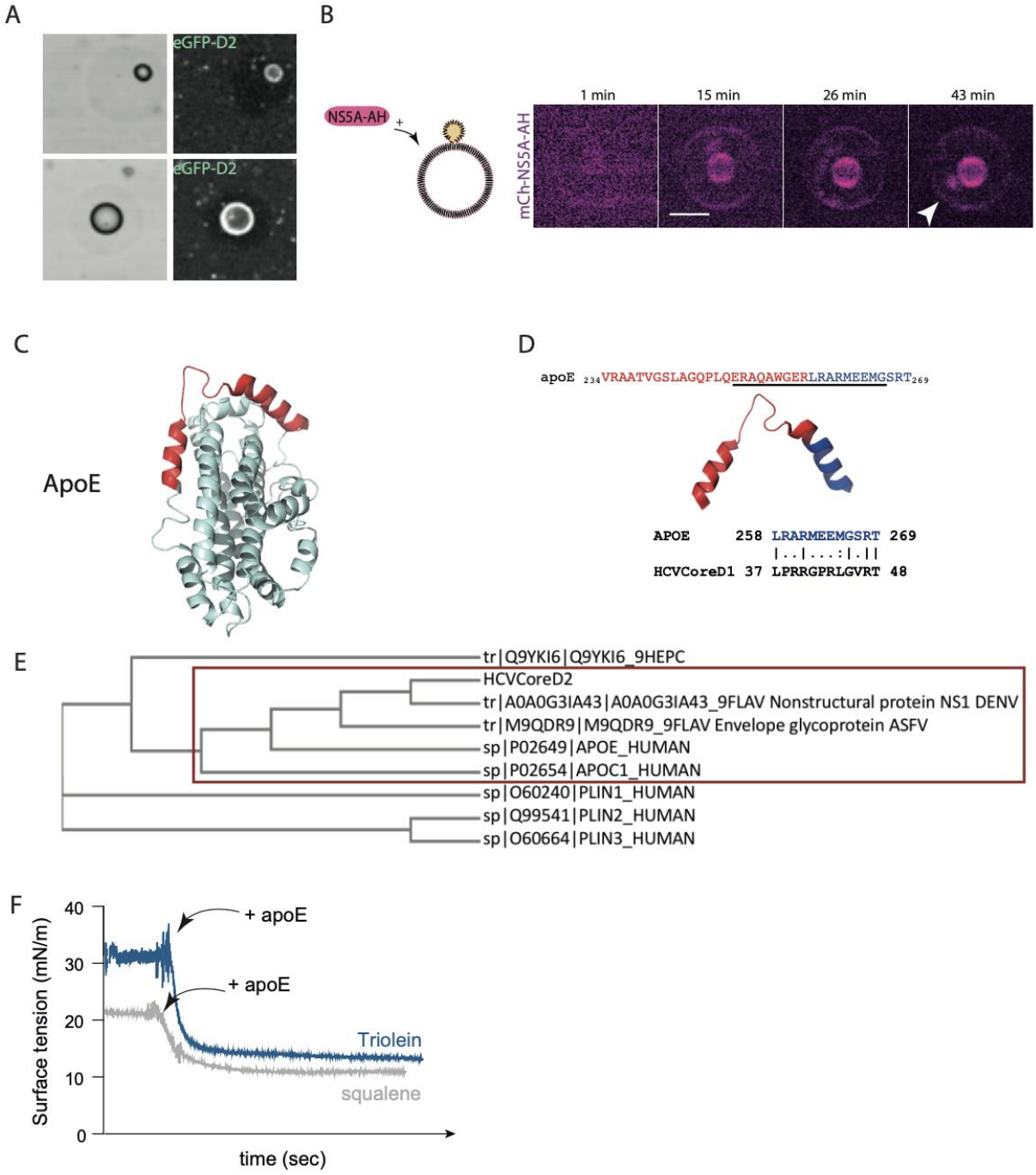
A
eGFP-D2
eGFP-D2
B
NS5A-AH
+
1 min
15 min
26 min
43 min
mCh-NS5A-AH
C
ApoE
D
apoE 234VRAATVGSLAGQPLQERAQAWGERLRARMEEMGSRT269
APOE 258 LRARMEEMGSRT 269
HCVCoreD1 37 LPRRGPRLGVRT 48
E
tr|Q9YKI6|Q9YKI6_9HEPC
HCVCoreD2
tr|A0A0G3IA43|A0A0G3IA43_9FLAV Nonstructural protein NS1 DENV
tr|M9QDR9|M9QDR9_9FLAV Envelope glycoprotein ASFV
sp|P02649|APOE_HUMAN
sp|P02654|APOC1_HUMAN
sp|O60240|PLIN1_HUMAN
sp|Q99541|PLIN2_HUMAN
sp|O60664|PLIN3_HUMAN
F
Surface tension (mN/m)
40
30
20
10
0
+ apoE
+ apoE
Triolein
squalene
time (sec)

Figure S6

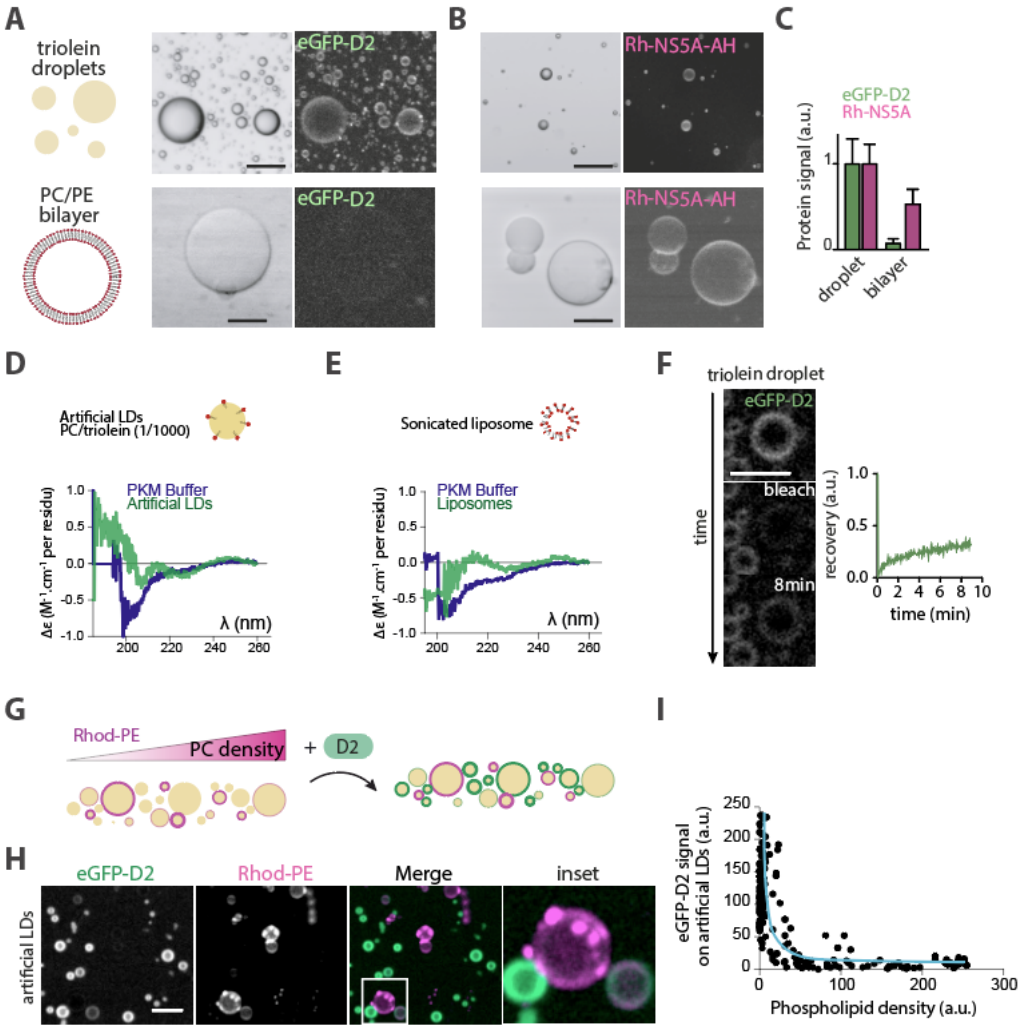

Figure 2

1216

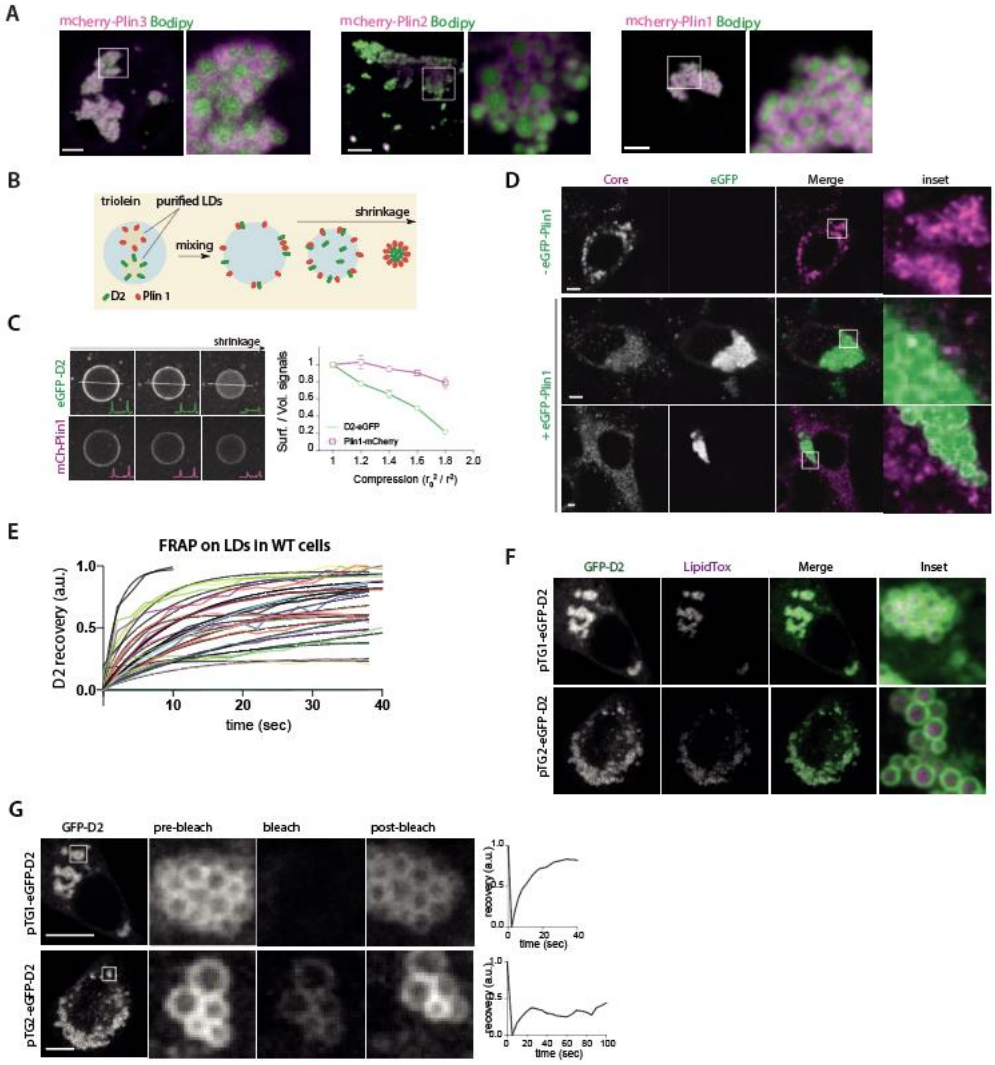

1217

Figure S3

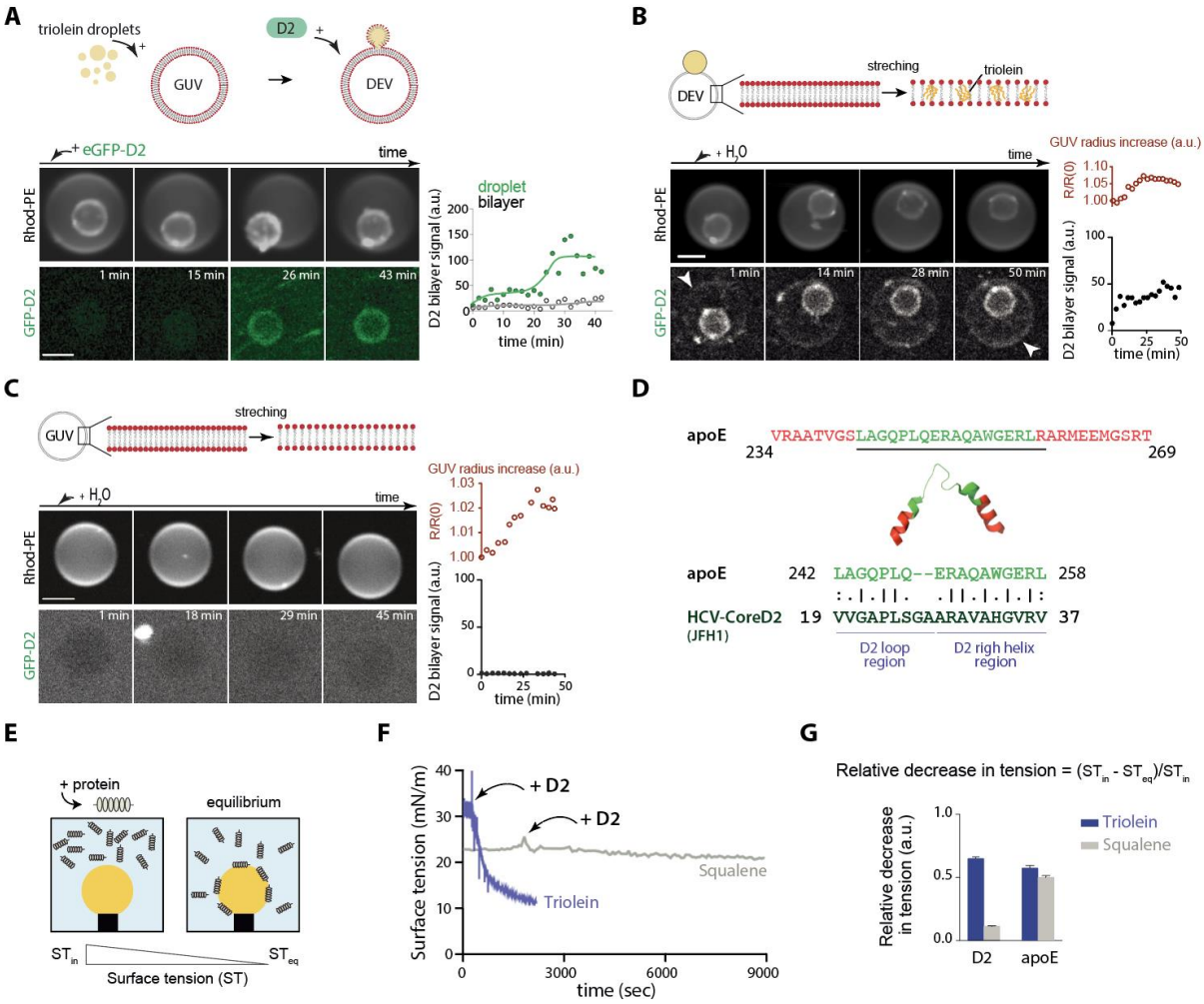

Figure 6

1218

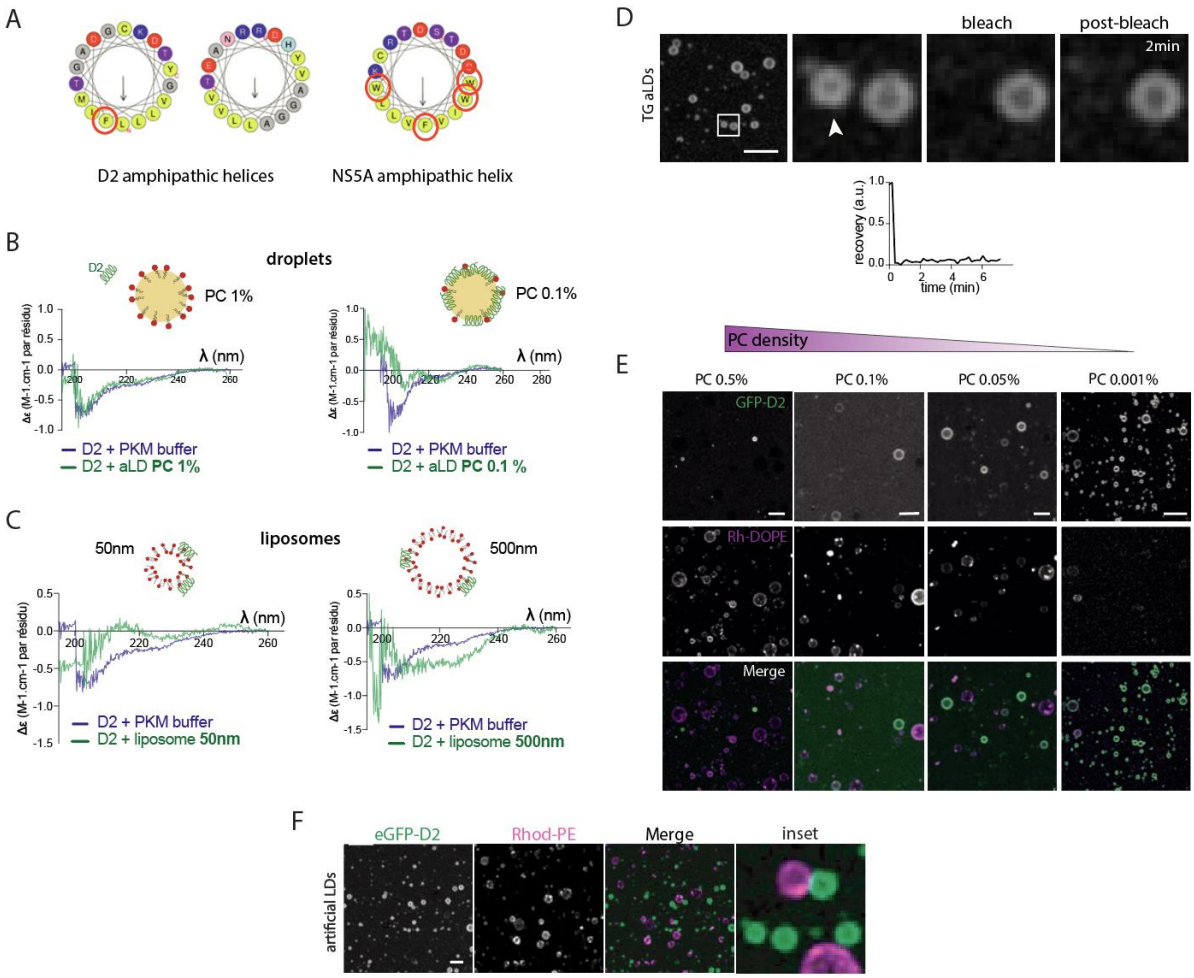
A
D2 amphipathic helices
NS5A amphipathic helix
B
droplets
D2
PC 1%
PC 0.1%
λ (nm)
Δε (M-1.cm-1 par résidu)
D2 + PKM buffer
D2 + aLD PC 1%
D2 + aLD PC 0.1 %
C
liposomes
50nm
500nm
D2 + liposome 50nm
D2 + liposome 500nm
D
bleach
post-bleach
2min
TG aLDs
recovery (a.u.)
time (min)
E
PC density
PC 0.5%
PC 0.1%
PC 0.05%
PC 0.001%
GFP-D2
Rh-DOPE
Merge
F
eGFP-D2
Rhod-PE
Merge
inset
artificial LDs

Figure S2

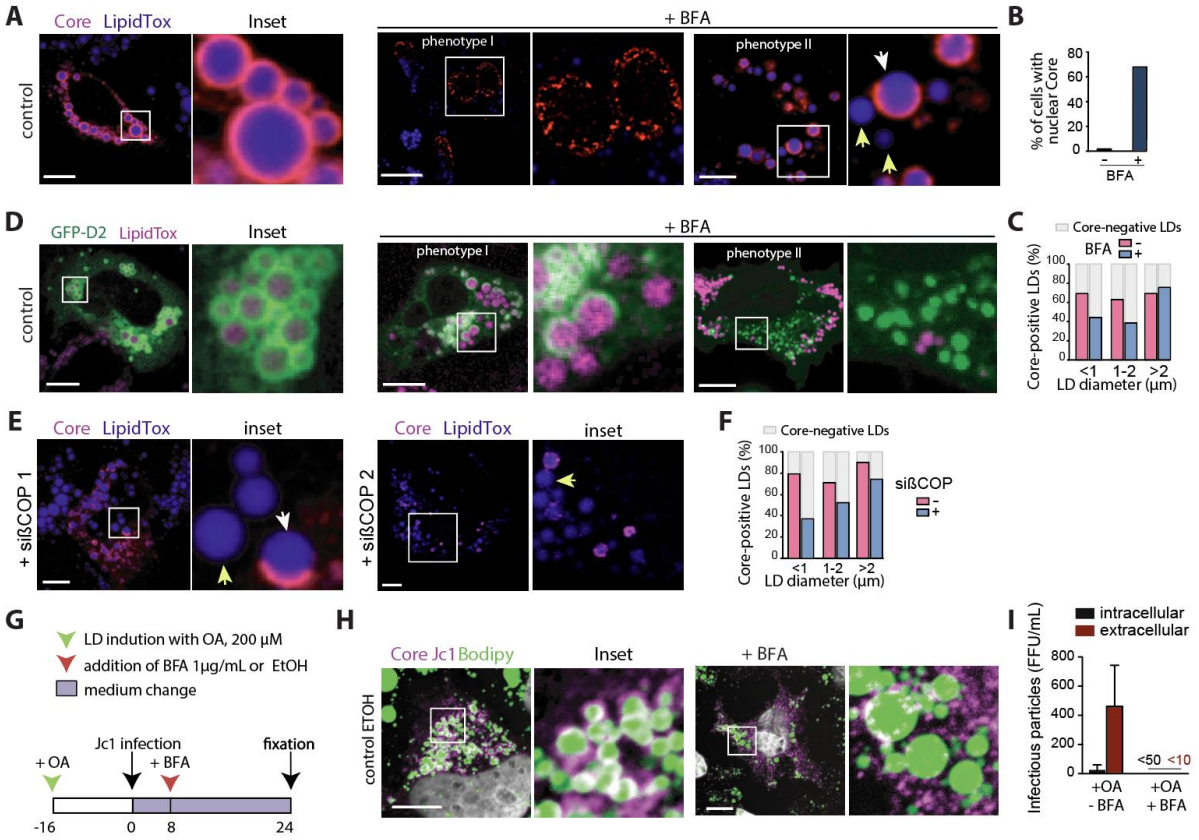
A
Core LipidTox
Inset
control
+ BFA
phenotype I
phenotype II
B
% of cells with nuclear Core
BFA
D
GFP-D2 LipidTox
Inset
control
+ BFA
phenotype I
phenotype II
C
Core-negative LDs
BFA
Core-positive LDs (%)
<1 1-2 >2
LD diameter (µm)
E
Core LipidTox
inset
+ sißCOP 1
Core LipidTox
inset
+ sißCOP 2
F
Core-negative LDs
Core-positive LDs (%)
sißCOP
<1 1-2 >2
LD diameter (µm)
G
LD indution with OA, 200 µM
addition of BFA 1µg/mL or EtOH
medium change
+ OA
Jc1 infection
+ BFA
fixation
-16
0
8
24
H
Core Jc1 Bodipy
Inset
+ BFA
control ETOH
I
intracellular
extracellular
Infectious particles (FFU/mL)
<50 <10
+OA - BFA
+OA + BFA

Figure 4

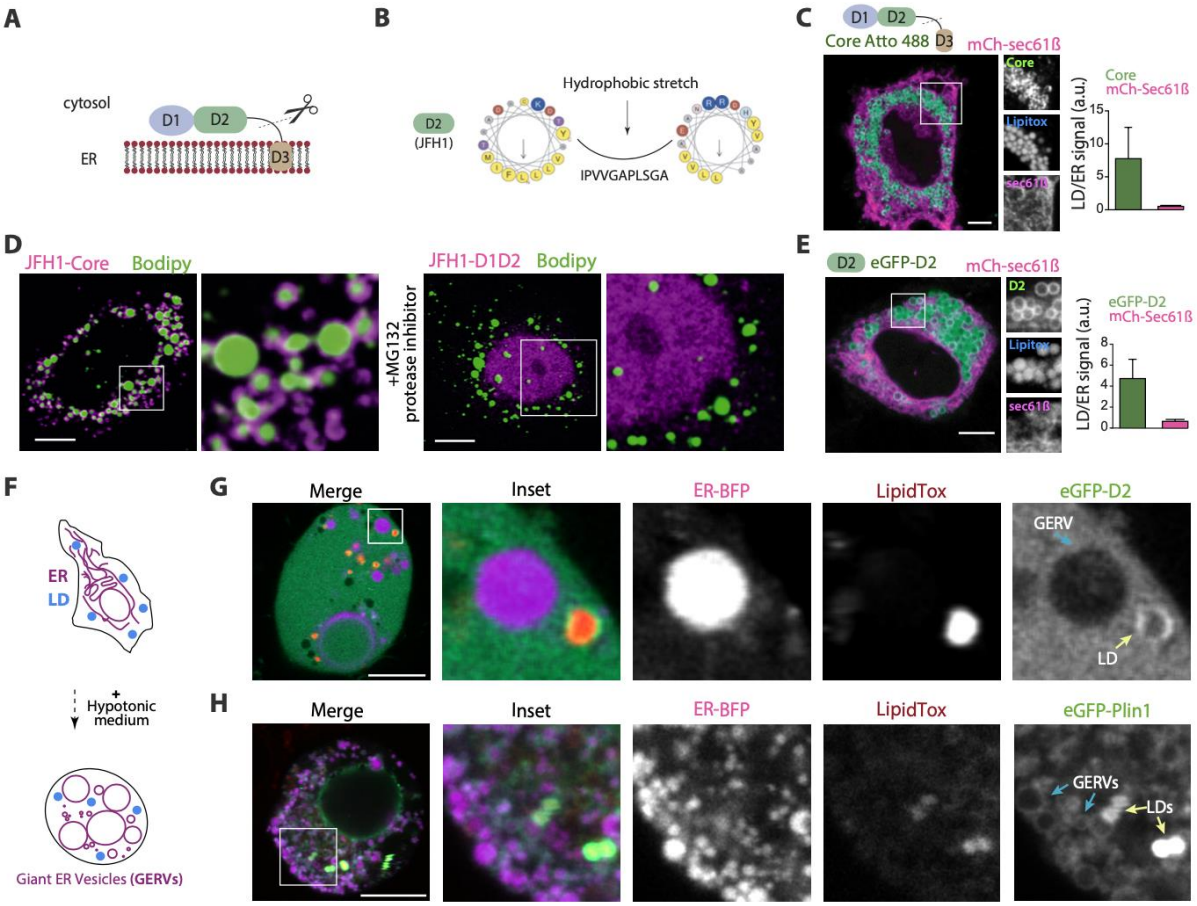

Figure 1

1221

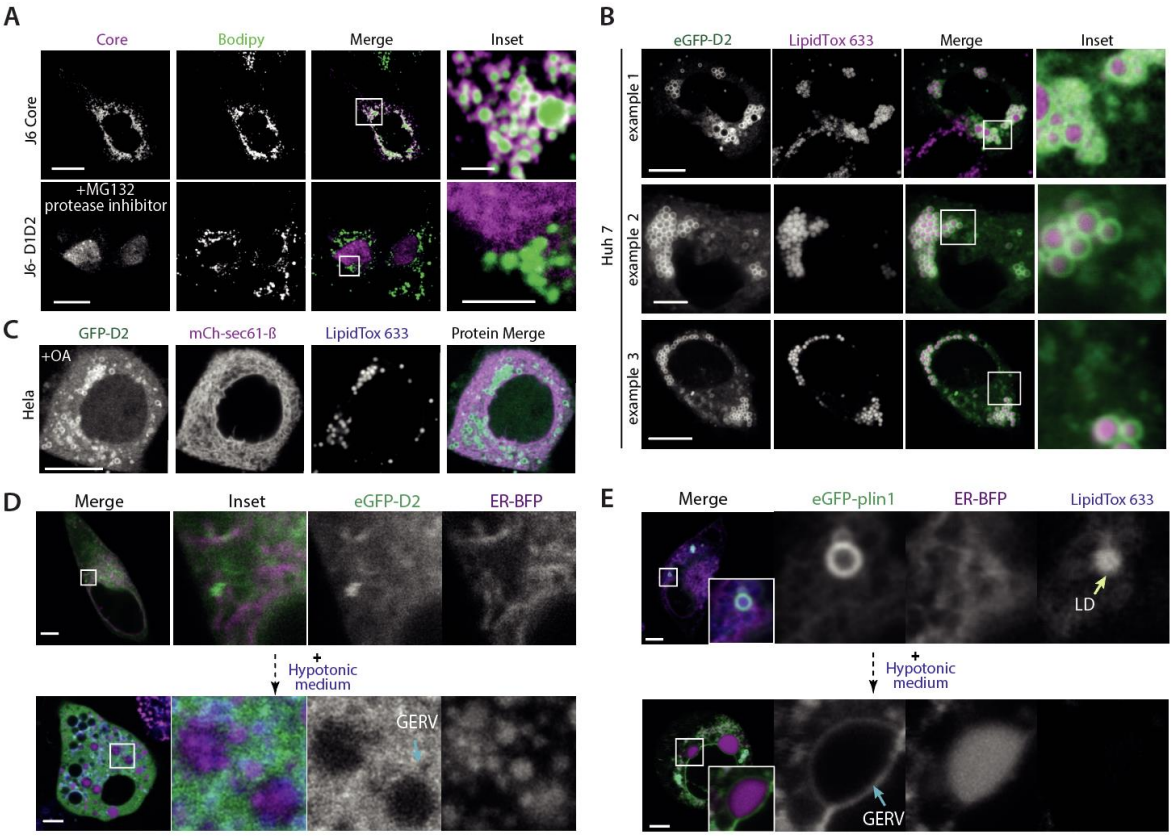

Figure S1

1222

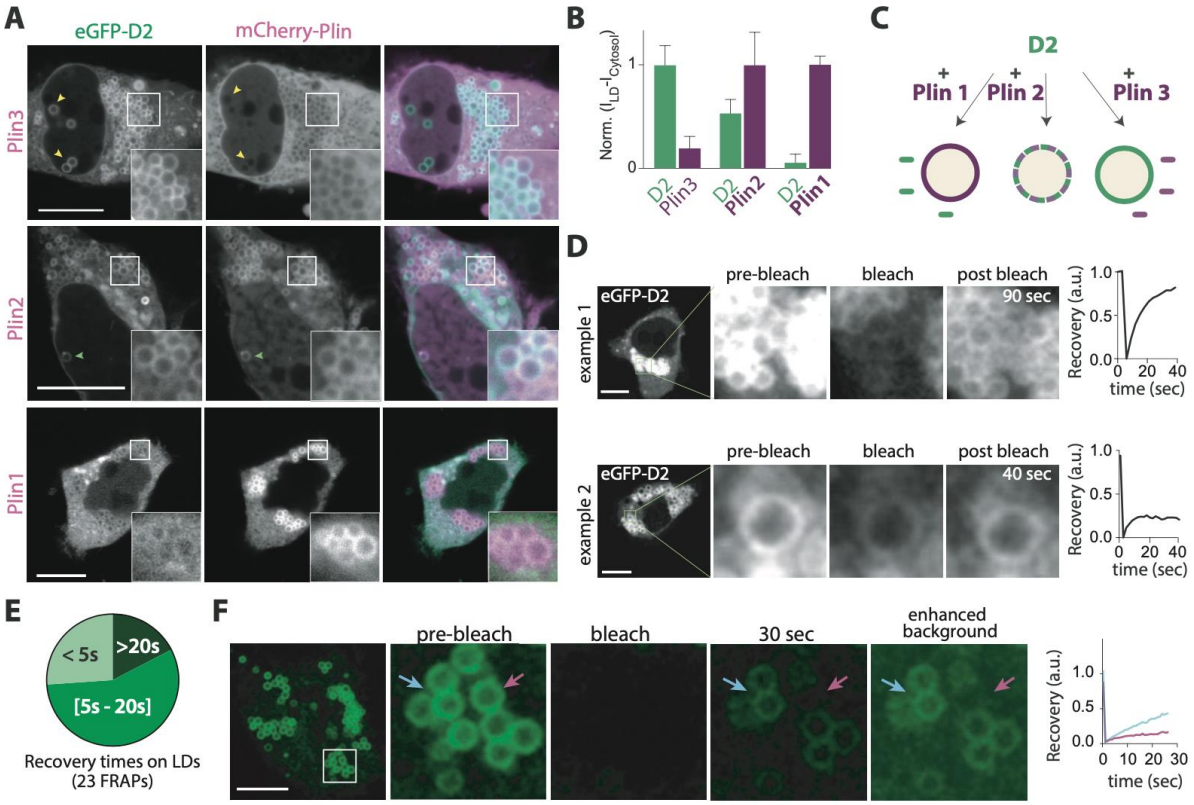

1223

Figure 3

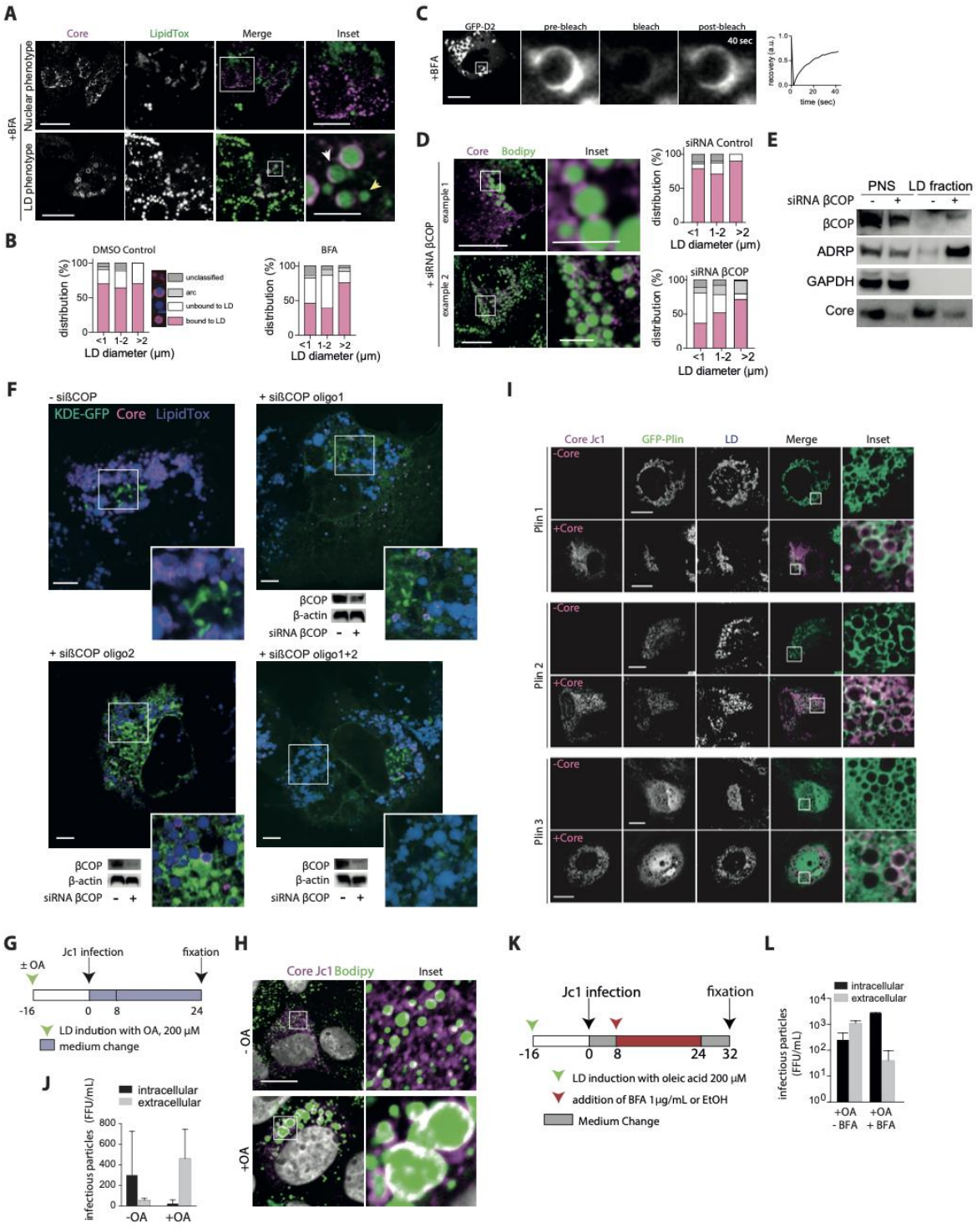
A
Core
LipidTox
Merge
Inset
+BFA
Nuclear phenotype
LD phenotype
B
DMSO Control
BFA
distribution (%)
unclassified
arc
unbound to LD
bound to LD
<1 1-2 >2
LD diameter (µm)
C
GFP-D2
pre-bleach
bleach
post-bleach
40 sec
recovery (a.u.)
time (sec)
D
Core Bodipy
Inset
+ siRNA βCOP
example 1
example 2
siRNA Control
siRNA βCOP
E
PNS
LD fraction
siRNA βCOP
βCOP
ADRP
GAPDH
Core
F
- sißCOP
KDE-GFP Core LipidTox
+ sißCOP oligo1
+ sißCOP oligo2
+ sißCOP oligo1+2
βCOP
β-actin
siRNA βCOP
I
Core Jc1
GFP-Plin
LD
Merge
Inset
Plin 1
Plin 2
Plin 3
-Core
+Core
G
± OA
Jc1 infection
fixation
-16
0
8
24
LD indution with OA, 200 µM
medium change
H
Core Jc1 Bodipy
Inset
-OA
+OA
J
intracellular
extracellular
infectious particles (FFU/mL)
-OA
+OA
K
Jc1 infection
fixation
-16
0
8
24
32
LD induction with oleic acid 200 µM
addition of BFA 1µg/mL or EtOH
Medium Change
L
intracellular
extracellular
infectious particles (FFU/mL)
+OA - BFA
+OA + BFA

Figure S4

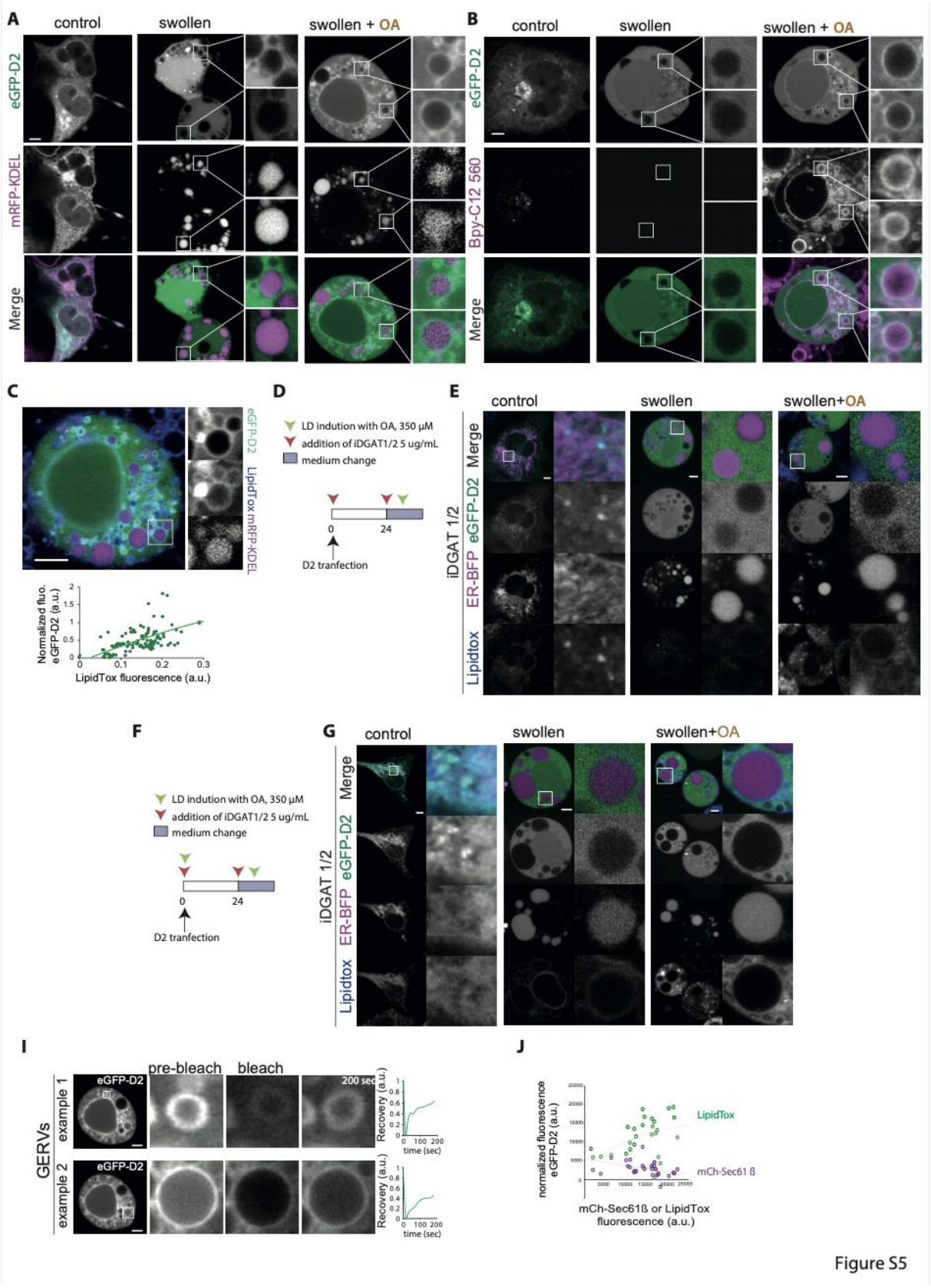
A
control
swollen
swollen + OA
eGFP-D2
mRFP-KDEL
Merge
B
control
swollen
swollen + OA
eGFP-D2
Bpy-C12 560
Merge
C
eGFP-D2
LipidTox mRFP-KDEL
Normalized fluo. eGFP-D2 (a.u.)
LipidTox fluorescence (a.u.)
D
LD indution with OA, 350 µM
addition of iDGAT1/2 5 ug/mL
medium change
0
24
D2 tranfection
E
control
swollen
swollen+OA
iDGAT 1/2
Merge
eGFP-D2
ER-BFP
Lipidtox
F
LD indution with OA, 350 µM
addition of iDGAT1/2 5 ug/mL
medium change
0
24
D2 tranfection
G
control
swollen
swollen+OA
iDGAT 1/2
Merge
eGFP-D2
ER-BFP
Lipidtox
I
pre-bleach
bleach
GERVs
example 1
example 2
eGFP-D2
200 sec
Recovery (a.u.)
time (sec)
J
normalized fluorescence eGFP-D2 (a.u.)
LipidTox
mCh-Sec61 ß
mCh-Sec61ß or LipidTox fluorescence (a.u.)

Figure S5

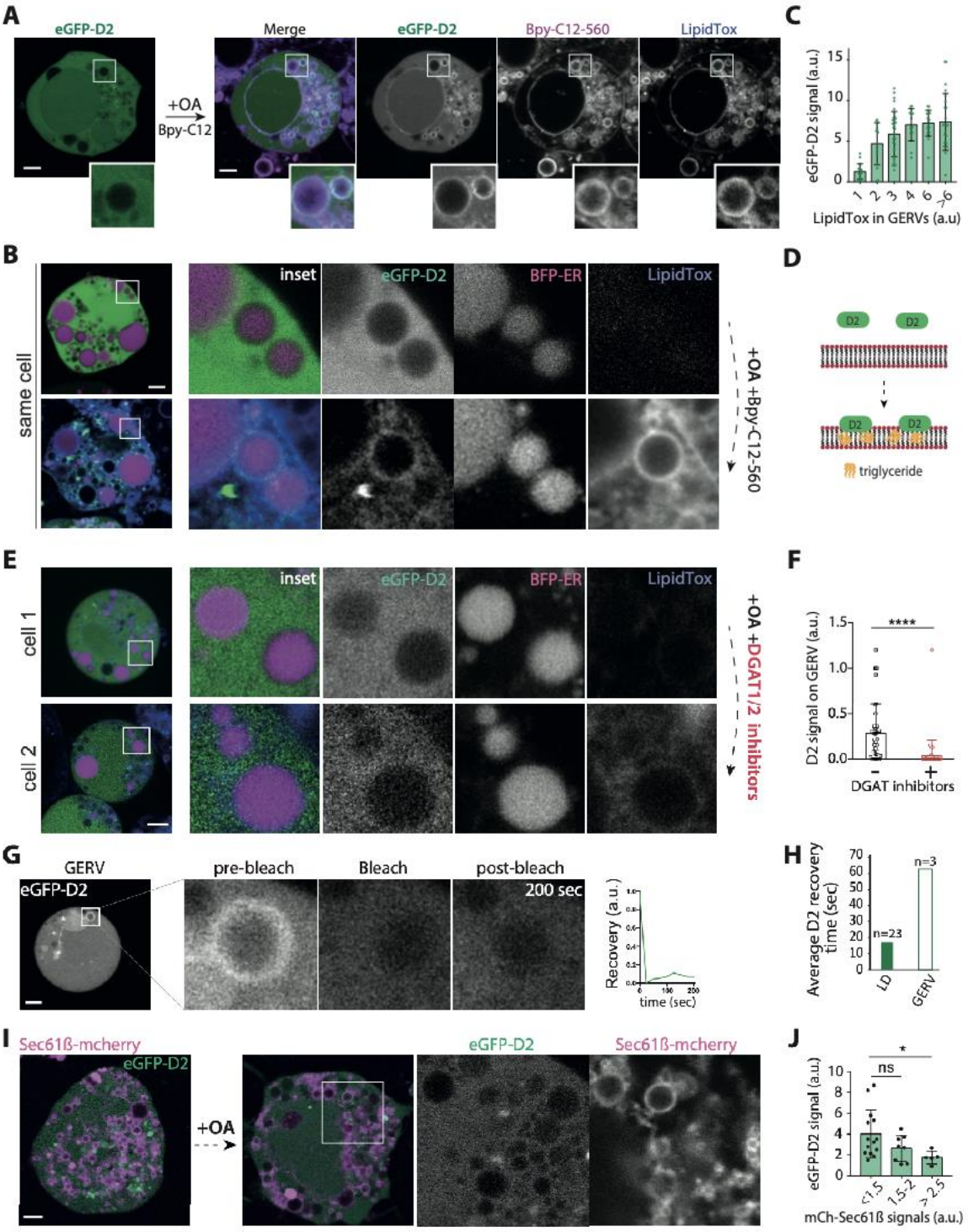
A
eGFP-D2
+OA
Bpy-C12
Merge
eGFP-D2
Bpy-C12-560
LipidTox
C
eGFP-D2 signal (a.u.)
LipidTox in GERVs (a.u)
B
same cell
inset
eGFP-D2
BFP-ER
LipidTox
+OA +Bpy-C12-560
D
D2
triglyceride
E
cell 1
cell 2
+OA +DGAT1/2 inhibitors
F
D2 signal on GERV (a.u.)
****
DGAT inhibitors
G
GERV
eGFP-D2
pre-bleach
Bleach
post-bleach
200 sec
Recovery (a.u.)
time (sec)
H
Average D2 recovery time (sec)
n=23
n=3
LD
GERV
I
Sec61ß-mcherry
eGFP-D2
+OA
J
ns
*
eGFP-D2 signal (a.u.)
mCh-Sec61ß signals (a.u.)

Figure 5